Heterogeneously randomized STZ model of metallic glasses: Softening and extreme value statistics during deformation

Pengyang Zhao [a,1], Ju Li [b,c,*,1], Yunzhi Wang [a,*]

[a] Department of Materials Science and Engineering, The Ohio State University, Columbus, OH 43210, USA
[b] Department of Nuclear Science and Engineering, MIT, Cambridge, MA 02139, USA
[c] Department of Materials Science and Engineering, MIT, Cambridge, MA 02139, USA

ARTICLE INFO

ABSTRACT

A nanoscale kinetic Monte Carlo (kMC) model is developed to study the deformation behavior of metallic glasses (MGs). The shear transformation zone (STZ) is adopted as our fundamental deformation unit and each nanoscale volume element (~1 nm voxel) in the MG is considered as a potential STZ that may undergo inelastic rearrangements sampled from a randomized catalog that varies from element to element, with stress-dependent activation energies. The inelastic transformation sampled out of spatially randomized catalogs (a key characteristic of glass) is then treated as an Eshelby's inclusion and the induced elastic field is solved in the Fourier space using the spectral method. The distinct features of our model, compared to previous work, are the introduction of randomized event catalogs for different nanoscale volume elements, repeated operations within the same element, and a "generation-dependent" softening term to reflect the internal structural change after each deformation. Simulations of uniaxial tension show the important effect of softening on the formation of shear bands, with a size-independent thickness of 18 nm. Statistical analysis of the accumulated strain at the ~1 nm voxel level is carried out and sample size effect on the extreme value statistics is discussed.

1. Introduction

Despite the localized deformation and poor ductility, metallic glasses (MGs) have exhibited many promising properties such as high yield strength, low friction coefficient and high resistance to corrosion, oxidation and wear (Trexler and Thadhani, 2010), and simulations at different levels have been performed to gain fundamental understanding of the mechanisms underlying these unique properties (Su and Anand, 2006; Vaidyanathan et al., 2001; Bulatov and Argon, 1994; Shimizu et al., 2006; Yang et al., 2006). Atomistic simulations such as molecular dynamics (MD) have offered a great view of the detailed configurations and energetics at the atomistic level (Takeuchi and Edagawa, 2011). However, issues such as shear banding which has a typical thickness of 10–100 nm (Shimizu et al., 2006, 2007; Shan et al., 2008; Sethi et al., 1978; Donovan and Stobbs, 1981; Pekarskaya et al., 2001; Li et al., 2002; Jiang and Atzmon, 2003) and formation time of 10^{-5}–10^{-3} s (Neuhauser, 1978; Hufnagel et al., 2002), are still not suitable for most MD simulations, and mesoscale models are needed to fill this gap.

By treating the plastic flow as a stochastic sequence of *local inelastic transformations*, or more commonly *shear transformation zones* (STZs) (Argon, 1979), Bulatov and Argon (1994) developed a model to simulate the elasto-plastic behavior in amorphous media. After assigning $\mathcal{M} = 6$ possible STZ transformations to each element (this event menu or catalog is

---

* Corresponding authors. Address: Department of Nuclear Science and Engineering, MIT, Cambridge, MA 02139, USA (J. Li).
  E-mail addresses: zhao.247@osu.edu (P. Zhao), liju@mit.edu (J. Li), wang.363@osu.edu (Y. Wang).
[1] These authors contributed equally to this work.

identical for all elements), the system was evolved according to kinetic Monte Carlo (kMC) algorithm (Bulatov and Argon, 1994). Although the event catalog is identical everywhere – or spatially homogeneous – thermal fluctuations can still randomize the system as time goes on, and load-shedding elastic interactions between volume elements bias the transformation activation energies $\{Q^{(m)}\}$, $m = 1 \ldots \mathcal{M}$ at each element to produce correlated deformation. Bulatov and Argon showed that shear bands can form, despite identical transformation catalogs and no internal softening in the model.

Homer and Schuh (2009) replaced the Green's function in Bulatov–Argon with finite element analysis (FEA) to solve the stress field, which allows modeling of more complex geometries and loading conditions. Also, the event catalog of each volume element contains infinite possibilities – but again identical everywhere – and they let thermal fluctuations and elastic interactions to break the symmetry. They have recently applied their model successfully to three-dimensional (3D) simulations as well (Homer and Schuh, 2010).

In this paper, we add two physical effects previously ignored. First, we will introduce "heterogeneously randomized" event catalogs, where each voxel (volume element) is "born different" (see Fig. 1). This follows from the disordered nature of the glass atomic structure. For instance, Srolovitz, Vitek and Egami used atomistic simulations to compute the distribution of atomic-level residual stress in a metallic glass, and found it to have a wide distribution (Srolovitz et al., 1983), with some volumes under significant compression and some under significant tension. For reasons like the above, while one voxel may be predisposed to a certain set of inelastic transformations, another voxel may be predisposed to a quite different set of transformations. Unlike typical representative volume element (RVE) approach in continuum mechanics modeling whose spatial coarse-graining volume is much larger than an atom, the voxels used in STZ kMC simulations have physical dimension of ∼1 nm to match the actual size of each STZ event (Argon, 1979), and so atomic-scale fluctuations or "predispositions" should survive at the mesoscopic voxel level. As a side remark, the fact that we assign a fixed length ∼1 nm on our voxel dimension means our modeling results may manifest a size dependence, i.e., dependence on the simulated physical sample size (Shan et al., 2008), in contrast to most continuum models based on "scale-free" consitutive laws and RVEs.

In a previous model (Baret et al., 2002) based on interface pinning/depinning, by allowing the local interfaces to slip in a random fashion, the plasticity of amorphous solids was described. However, the disordered nature of an amorphous solid was reflected solely in the long-range elastic interactions. In contrast, the heterogeneous STZ catalog introduced in our model captures such a disordered nature in both the long-range elastic interactions and the potential energy landscape that defines the transformation pathways.

The second physical effect is strain-induced softening which has been observed experimentally (Xi et al., 2005; Bei et al., 2006; Nagendra et al., 2000). As illustrated in Fig. 1, once a generation-0 (untransformed) voxel has undergone a certain shear transformation, it possesses a new internal structure, which we call generation-1. A new catalog of transformation opportunities should be presented to this generation-1 voxel, different from those for generation-0, even though the two generations sit at the same location (Lagrangian reference frame). Generally speaking, from the works of Spaepen and others (Spaepen, 1977; Su and Anand, 2006), we believe that the activation barriers $\{Q^{(m)}\}$ tend to be *lowered* for generation-1 as compared to generation-0, under identical external conditions (namely stress and temperature), due to internal structural changes (Shimizu et al., 2006) termed "free-volume creation" by Spaepen. This shear softening, closely related to the formation of shear band, is also believed to be responsible for many other critical issues such as local heating (Lewandowski and Greer, 2006), nano-void formation (Li et al., 2002), and nanocrystallization (Chen et al., 1994). The instability nature of softening helps to develop some "extreme sites" which undergo intense plastic deformation and cavitation that finally lead to fracture (Shimizu et al., 2006; Shimizu et al., 2007). Thus it is crucial to understand the role played by the generation-dependent softening in deformation of MGs, especially at current stage when lots of attempts have been made trying to improve mechanical properties such as ductility and toughness (Ritchie, 2011). In addition, the experimentally confirmed short (medium)-range ordering (Hirata et al., 2011) and bonding anisotropy during creep (Suzuki et al., 1987) suggest that softening at
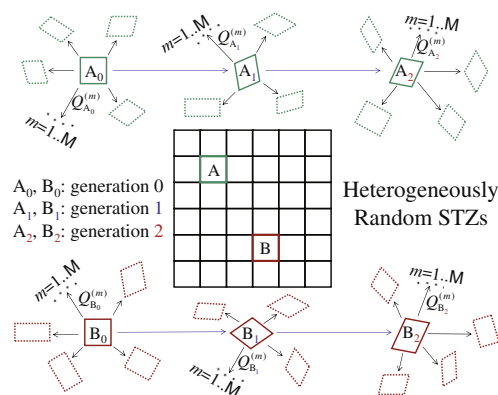
Fig. 1. Illustration of the heterogeneously randomized STZ model (to be contrasted with Fig. 1(b) of Bulatov and Argon (1994)). $Q^{(m)}$ is the activation free energy for a voxel to transform in the mth mode.

mesoscale could involve some structural changes of atomic clusters, and this leads us to a *directional* softening scheme, which will be detailed in the following. Finally, the metastable nature of MGs will inevitably raise the question of structural relaxation, serving as a competition with softening, which will also be included in our model based on a recent experimental study (Dubach et al., 2007).

From the point of view of physics-based simulations, there are three physical effects we would like to explore and understand regarding the propensity to form shear bands: (a) heterogeneous catalogs, (b) generation-dependent softening, and (c) thermally activated transformations and load-shedding interactions. Very crudely, we would expect (a) to retard shear band formation, while (b) and (c) to favor shear band formation. This is because shear band is defined as a *very collective flow defect with long aspect ratio*, where the many voxels within the same shear band are dominated by inelastic shear strains of approximately the *same* character. While the elastic interaction kernel in (c) promotes such strong correlations, having (a) should delay it somehow, since the transformation strains in each voxel cannot be perfectly aligned even if they want to (in contrast to Fig. 1(b) of Bulatov and Argon (1994), where they can). Feature (c) is common among all STZ kMC models (Bulatov and Argon, 1994; Homer and Schuh, 2009) – it focuses on change of the *external* environment, namely the stress, on the future transformations of a voxel; while (a) and (b) focus on the influence of the *internal state* of this voxel on its own future transformations. Information regarding (a) and (b) in principle can be provided by detailed atomistic calculations of the topology of energy-basin network in phase space (Hara and Li, 2010; Li et al., 2011), and handed off to the STZ kMC model in a multiscale scheme. However, even an empirical parametric study at the STZ dynamics level, respecting all mechanical symmetry and causality requirements, may reveal interesting physics (see some applications of mesoscopic models of MGs in a recent review paper (Rodney et al., 2011)). This is the approach we will take in this paper.

2. Methodology

Here we present an empirical mesoscale numerical model that incorporates (a) heterogeneous catalogs and (b) generation-dependent softening ("rejuvenation" of glass (Wolynes, 2009)) and counteracting structural recovery process ("aging" of glass (Wolynes, 2009)). The STZ theory (Argon, 1979) is employed to describe the fundamental deformation in BMGs and the resultant elastic field is solved in Fourier space in light of the faster convergence than in real space. Due to different state configurations (stress distribution, local softening, etc.), the response to external field may be classified as pure elasticity, thermal plasticity, or athermal plasticity, and kMC algorithm is used to simulate the dynamics.

2.1. Deformation mechanism

2.1.1. Shear transformation zone

A widely accepted picture of deformation in MG is based on the concept of shear transformation zone (STZ), first proposed by Argon (1979) and supported by MD simulations (Falk and Langer, 1998). A STZ is essentially a cluster of local atoms of volume V moving in a collective manner to accommodate shear (Schuh and Lund, 2003; Schuh et al., 2007), with $V = 1 \sim 10^2$ atomic volumes (Argon, 1979; Johnson and Samwer, 2005; Mayr, 2006; Pan et al., 2008). One can use the real time t to index the condition of this cluster, for example, $V(t)$ to describe possible dilatancy. However, it is often conceptually advantageous also to use an integer index g ("generation") to label the condition of this cluster, with $g = 0$ denoting the initial configuration of this cluster of atoms at $t = 0$, when the macroscopic deformation begins. A generation change ($g: 0 \rightarrow 1$, or $1 \rightarrow 2$) is deemed to have taken place when there is an "essential" change in the cluster's atomic geometry, after the "trivial" thermal vibrations and elastic displacements are filtered out. This can be more precisely defined by the following domain-decomposition scheme. We regard the entire material as consisting of the cluster atoms of interest, whose positions are denoted by a long vector $\mathbf{x}^{\text{cluster}}$, and the rest of the atoms, who positions are denoted by an even longer vector $\mathbf{x}^{\text{environ}}$. The potential energy landscape is a function of both $\mathbf{x}^{\text{cluster}}$ and $\mathbf{x}^{\text{environ}}$:

$$U = U(\mathbf{x}^{\text{cluster}}, \mathbf{x}^{\text{environ}}) \tag{1}$$

However, we take Eshelby's stance that when "interesting" things happen within the cluster, the environment responds, but only in a thermo-elastic manner, i.e. the plasticity or inelasticity is localized within the cluster, whereas the surrounding medium behaves elastically (Eshelby, 1957). That is to say, we can perform quadratic expansion on $\mathbf{x}^{\text{environ}}$:

$$U = u(\mathbf{x}^{\text{cluster}}) + \frac{(\mathbf{x}^{\text{environ}} - \mathbf{X}(\mathbf{x}^{\text{cluster}}))^T \mathbf{K}(\mathbf{x}^{\text{cluster}})(\mathbf{x}^{\text{environ}} - \mathbf{X}(\mathbf{x}^{\text{cluster}}))}{2} + \cdots \tag{2}$$

where $\mathbf{X}(\mathbf{x}^{\text{cluster}})$ is the equilibrium position vector of the environment atoms as they are being "dragged" by the cluster atoms, and $\mathbf{K}(\mathbf{x}^{\text{cluster}})$ is their instantaneous stiffness. $\mathbf{K}(\mathbf{x}^{\text{cluster}})$ is a positive definite matrix - if this is not the case, one can simply enlarge the definition of the cluster, until $\mathbf{K}$ is positive definite, i.e., the energy landscape that $\mathbf{x}^{\text{environ}}$ sees is always convex to allow expansion Eq. (2). The quality of the approximate energy landscape Eq. (2) of course depends on the definition of the "cluster" atoms. If the cluster volume is much greater than the activation volume (Hara and Li, 2010; Zhu and Li, 2010; Li, 2007), we expect the approximation quality to get better and better. Even though dim($\mathbf{x}^{\text{environ}}$) ≫ dim($\mathbf{x}^{\text{cluster}}$), its role in $U(\mathbf{x}^{\text{cluster}}, \mathbf{x}^{\text{environ}})$ is to serve as a "trivial" thermo-elastic surrounding medium, and so these degrees of freedom can

be integrated out in the partition function in statistical thermodynamics. One can therefore define a constrained free energy for the cluster as:

$$f(\mathbf{x}^{\text{cluster}}) \equiv -k_\text{B}T \ln \int d\mathbf{x}^{\text{environ}} e^{-U/k_\text{B}T} + \text{const} = u(\mathbf{x}^{\text{cluster}}) + k_\text{B}T \sum_j \ln \frac{\hbar}{k_\text{B}T} \sqrt{\frac{K_j}{m}}, \tag{3}$$

where K_j is the jth eigenvalue of $\mathbf{K}(\mathbf{x}^{\text{cluster}})$ matrix that is always positive, $\hbar$ is the Planck constant, k_B is the Boltzmann constant, T is the temperature, and m is the geometric-mean atomic mass of the environment atoms. In Eshelby's original formulation, he in fact also took the medium stiffness to be a cluster-independent constant (Eshelby, 1957)

$$\mathbf{K}(\mathbf{x}^{\text{cluster}}) = \mathbf{K} \tag{4}$$

resulting in an elasticity expression for the quadratic term. The purpose of Eq. (2)–(4) is to demonstrate that for discussing certain events, the full energy landscape $U(\mathbf{x}^{\text{cluster}}, \mathbf{x}^{\text{environ}})$ can be well-approximated by a much smaller dimensional free-energy landscape $f(\mathbf{x}^{\text{cluster}})$.

Armed with this "smaller" free-energy landscape $f(\mathbf{x}^{\text{cluster}})$, we can perform stability analysis on $\mathbf{x}^{\text{cluster}}$. A contiguously convex region of $f(\mathbf{x}^{\text{cluster}})$ is called a "basin" for this STZ, which must contain a single local minimum. If $\mathbf{x}^{\text{cluster}}(t)$ moves within the confines of a single basin, this is defined as thermo-elastic motion, and the cluster geometry is considered to be of the same generation. However, weakened by the local stress $\boldsymbol{\sigma}$ and hit by a thermal fluctuation "rogue wave" of colliding phonons, the cluster geometry may occasionally switch basin. In order to switch basin, it must pass through non-convex region of $f(\mathbf{x}^{\text{cluster}})$, even if temporarily. A generation change is defined to happen when the cluster geometry changes from one basin to another, after passing through non-convex region of $f(\mathbf{x}^{\text{cluster}})$ (so-called activated states) where one or more eigenvalues of the 2nd-derivative matrix are negative. The definitions above are quite similar to the concept of inherent structures (Stillinger and Weber, 1982) and hopping between inherent structures (Li et al., 2011), but applied to a local cluster instead of an entire atomic system, via schemes of domain decomposition and the Eshelby approximation Eqs. (2)–(4). This serves as the basis for the STZ theory.

Now, imagine a large domain of MG under an average stress $\bar{\boldsymbol{\sigma}}$, in which this cluster is embedded. The generation $g \to g+1$ change of this cluster (see Fig. 1 illustration) is called a *transformation*, using the language of Eshelby transformation (Eshelby, 1957). In reference to the generation-g cluster, the transformed cluster has transformation strain $\boldsymbol{\varepsilon}_{g \to g+1}$. (A computational procedure can be devised to define this strain tensor in terms of atomic geometries (Shimizu et al., 2007; Hara and Li, 2010)). Here, both the generation-g and the $g+1$ cluster geometries are in locally stable equilibrium states. Generally speaking, $\text{Tr}(\boldsymbol{\varepsilon}_{g \to g+1}) \neq 0$. However, the word "shear" in "shear transformation zone" theory means that many people believe $\boldsymbol{\varepsilon}_{g \to g+1}$ is shear-dominant, and as an approximation, we will also take

$$\text{Tr}(\boldsymbol{\varepsilon}_{g \to g+1}) = 0 \tag{5}$$

in this paper to simplify the modeling, although it is clear that when cavitation happens, approximation Eq. (5) will not hold. Also, $\boldsymbol{\varepsilon}_{g \to g+1}$ should depend on $\bar{\boldsymbol{\sigma}}$, but since

$$\boldsymbol{\varepsilon}_{g \to g+1}(\bar{\boldsymbol{\sigma}}) = \boldsymbol{\varepsilon}_{g \to g+1}(\bar{\boldsymbol{\sigma}} = 0) + \mathcal{O}(\bar{\boldsymbol{\sigma}}), \tag{6}$$

the $\mathcal{O}(\bar{\boldsymbol{\sigma}})$ term's impact on energy difference occurs on the second order in $\bar{\boldsymbol{\sigma}}$, and is frequently ignored. So in this paper we will also take the approximation that

$$\boldsymbol{\varepsilon}_{g \to g+1}(\bar{\boldsymbol{\sigma}}) = \boldsymbol{\varepsilon}_{g \to g+1}(\bar{\boldsymbol{\sigma}} = 0), \tag{7}$$

although this approximation will start to break down when "ideal strength" of glass is approached (Tian et al., 2012).

A saddle-point configuration in the free-energy landscape $f(\mathbf{x}^{\text{cluster}})$ must connect these two locally stable equilibrium states (generation-g and $g+1$). From now on we will use superscript $*$ to denote saddle-point properties. Using generation-g cluster as the reference state, we can also define volume of the saddle-point cluster geometry $V^*_{g \to g+1}$ and the strain tensor $\boldsymbol{\varepsilon}^*_{g \to g+1}$, when the cluster is at this in-between state. It is well appreciated that even when approximation Eq. (5) is exact as in crystal physics (Fig.1 of Li et al. (2003)), there could be dilatation involved at the saddle point:

$$V^*_{g \to g+1} = V_g \det |\mathbf{I} + \boldsymbol{\varepsilon}^*_{g \to g+1}| \neq V_g \tag{8}$$

where V_g is the volume of the generation-g cluster.

In Eshelby (1957), Eshelby presented a famous result that in the case of an ellipsoidal inclusion, the actual transformation strain tensor distribution is (i) constant inside the inclusion, and (ii) proportional to the so-called stress-free transformation strain (SFTS) $\boldsymbol{\epsilon}_{g \to g+1}$:

$$\boldsymbol{\varepsilon}_{g \to g+1} = \mathcal{S} \boldsymbol{\epsilon}_{g \to g+1} \tag{9}$$

where the $\mathcal{S}$ is a rank-four tensor, often known as Eshelby tensor, and is constant for the ellipsoidal inclusion. In the present work we will pretend that our STZ is ellipsoidal, to take advantage of the constancy and the proportionality, even though ellipsoidal inclusions are obviously not space-filling. Under this assumption, the proportionality also ensures that the transformation strain $\boldsymbol{\varepsilon}_{g \to g+1}$ defined here is equivalent to SFTS $\boldsymbol{\epsilon}_{g \to g+1}$ in characterizing the inelastic nature of a generation change.

However, because $\boldsymbol{\varepsilon}$ always describes the actual transformation strain, we will use its *accumulated* value to describe the current strain field of the system and use $\boldsymbol{\epsilon}$ to describe the transformation modes for a generation change.

The notation system $\boldsymbol{\varepsilon}_{g\to g+1}$, $\boldsymbol{\epsilon}_{g\to g+1}$, $\boldsymbol{\varepsilon}^*_{g\to g+1}$, $V^*_{g\to g+1}$ is unambiguous but cumbersome. From now on we will adopt a shorthand:

$$\boldsymbol{\varepsilon}_g \equiv \boldsymbol{\varepsilon}_{g\to g+1}, \quad \boldsymbol{\epsilon}_g \equiv \boldsymbol{\epsilon}_{g\to g+1}, \quad \boldsymbol{\varepsilon}_{g*} \equiv \boldsymbol{\varepsilon}^*_{g\to g+1}, \quad V_{g*} \equiv V^*_{g\to g+1} \tag{10}$$

and sometime may even omit the g index:

$$\boldsymbol{\varepsilon} \equiv \boldsymbol{\varepsilon}_g, \quad \boldsymbol{\epsilon} \equiv \boldsymbol{\epsilon}_g, \quad \boldsymbol{\varepsilon}_* \equiv \boldsymbol{\varepsilon}_{g*}, \quad V_* \equiv V_{g*} \tag{11}$$

if the context is clear.

To determine the activation energy barrier that characterizes the STZ transformation, one needs to define the saddle-point configuration, namely $\boldsymbol{\varepsilon}^*_g$. In the absence of external stress, the activation energy barrier is then equal to the Helmholtz free energy difference between initial and saddle-point configurations ΔF_*, which can be considered as the total energy stored in the system if the system is flexed into the saddle-point in a quasi-equilibrium manner (Argon, 1996). If the inclusion happens to be spherical (as in the case of Homer–Schuh model (Homer and Schuh, 2009)), an analytical solution for ΔF_* exists and is detailed in Appendix A. For the purpose of an empirical parametric study, however, the exact form of ΔF_* is of little significance compared to the incorporated physical effects. We take $\Delta F_* = 5$ eV (the typical value for ΔF_* is $1 \sim 5$ eV, or $20 \sim 120$ $k_B T_g$ with T_g being the glass transition temperature (Schuh et al., 2007)) with certain fluctuation due to the elevation, tilt, and roughness in the energy landscape.

The actual activation barriers $\{Q^{(m)}\}$ in Fig. 1, when the applied stress is much smaller than $\hat{\tau}$, are linearized as Argon (1996)

$$Q^{(m)} = \Delta F_* - \frac{1}{2} V \sigma_{ij} \epsilon_{ij}^{(m)} \tag{12}$$

where the second term represents the tilt of the basin of STZ in the presence of local stress σ_{ij} and is essentially the work done during transformation. $\epsilon_{ij}^{(m)}$ is the SFTS tensor for the corresponding transformation mode. The factor $\frac{1}{2}$ is due to the assumption that at saddle point half of inelastic rearrangement is achieved. The transformation paths are then fully characterized by energy barriers defined in Eq. (12) for a "state-to-state" dynamics.

2.1.2. Event catalogs: STZ modes

The SFTS tensor $\boldsymbol{\epsilon}^{(m)}$, which characterize $\mathcal{M}$ different transformation modes for a generation change, are the input to a kMC STZ dynamics model. This is similar to the phase-field method in simulating phase transitions in alloys (Wang and Li, 2010) where the SFTS is calculated according to lattice correspondence determined by experimental characterization of orientation relationship and crystallographic theory of lattice rearrangement. In crystals, due to translational invariance, the number of variants and hence the number of transformation strain modes is determined by the group-subgroup relationship between the parent and product phase and, thus, is limited. For MG, the SFTS tensor, as mentioned previously, can be calculated through MD simulations (Shimizu et al., 2007; Hara and Li, 2010). In fact, this computational procedure can also be applied to crystals as well. The inherent atomic structure of systems in question, whether crystalline or amorphous, can only be rendered through the possible catalog for transformations, or STZ *modes*, shown as the $\mathcal{M}$ different "variants" in Fig. 1 for each generation.

In Bulatov–Argon model (Bulatov and Argon, 1994) an identical set with finite modes ($\mathcal{M} = 6$) is assigned to each element and is constant throughout the time evolution. This implies an event catalog which is spatially homogeneous and *generation-independent*. This is also the case for Homer–Schuh model (Homer and Schuh, 2009), even though their event catalog is replaced with one containing infinite modes. The spatially homogeneous and generation-independent catalogs for STZ transformations suggest that the simulated systems in both models are more like "crystals" rather than amorphous.

Following the work of Srolovitz et al. (1983) who showed a wide distribution of atomic-level residual stress, we introduce here "heterogeneously randomized" event catalogs such that each element is predisposed to its own *unique* set of STZ transformations, suggesting different "personalities" among the same generation. This is illustrated in Fig. 1 where for each generation $(0, 1, \ldots)$ elements at different locations $(A, B, \ldots)$ is "destined" to different transformation paths. The reason that there is only $\mathcal{M}$ finite modes rather than infinite as in Homer–Schuh is based on the consideration that the characteristic *isotropy* of long-range ordering (LRO) in MG is not necessarily to be preserved at STZ length scale. In fact, recent observation of diffraction patterns from local atomic clusters and their assemblies provides direct evidence on the local atomic order in BMGs (Hirata et al., 2011), implying that, on scale of an STZ size, it is unrealistic to expect a fully isotropic structure. The local atomic order will place certain constraints on allowed inelastic transformations, suggesting a finite event catalog.

In addition, it is necessary for event catalogs to be evolved during the generation evolution. In Fig. 1, for instance, the transformation modes for element A are always updated during the generation change $A_0 \to A_1 \to A_2$. This idea can be understood more clearly by first making an assumption that there exists a "coarse-grained" free energy $f(\boldsymbol{\epsilon})$ which preserves all the basins in $f(\mathbf{x}^{cluster})$. The generation changes can then be schematically shown as in Fig. 2(a) where the solid circles are the basins corresponding to the transformations in the event catalog and different colors represent different generations. The distribution of event catalogs is evolved as generation goes on, but statistically it follows an isotropic manner in the strain space as shown in Fig. 2(b). In this way the isotropy of LRO in MG is preserved in a statistical manner.
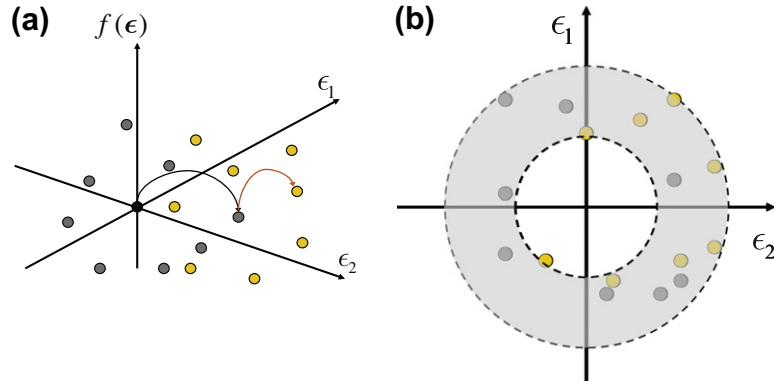
Fig. 2. (a) STZ transformations occur among basins of the energy landscape in the stress-free strain ϵ space denoted as solid circles with different colors assigned to different generations. ϵ_1 and ϵ_2 schematically represent all the strain axes. If converted into same reference, the SFTS tensors during generation changes will distribute isotropically in the strain space, illustrated as a "ring" region shown in (b).

It should be pointed out that in general, $\mathcal{M}$ needs not to be the same for every generation. However, for the purpose of our study, even a constant $\mathcal{M}$ is ready to provide the expected physical effects, and for simplicity we assume $\mathcal{M}$ is constant through the generation change. Then the physical meaning of $\mathcal{M}$ is restricted to the spatial heterogeneity of event catalogs. Considering the limit case of $\mathcal{M} \to \infty$, the catalog essentially becomes spatially homogeneous again. Thus we are expecting that the delaying of shear band formation due to heterogeneous catalogs will be erased as $\mathcal{M}$ becomes sufficiently large.

As regards the modeling aspect, we employ a numerical method to create those event catalogs to exhibit the "heterogeneous" and "randomized" features. More specifically, the SFTS tensors, which constitute an event catalog, are generated through certain statistical approach such that the *distribution* of resulted tensors is indistinguishable from that viewed in a rotated frame. Catalogs for each element at any generation are all obtained through this procedure, implying *isotropy* is preserved in both spatial and generation sense. In 2-dimension (2D) it is found that Gaussian distribution would satisfy our requirement (see the detail of the proof in Appendix B), and in fact atomistic simulations have shown a Gaussian-like distribution of plastic strains during the thermally activated plastic events in a flowing glass (Rodney and Schuh, 2009).

### 2.1.3. Generation-dependent softening

Shear localization is essentially the result of some inherent softening process which makes the deformed material more vulnerable to further plastic deformation, and eventually leads to a catastrophic failure. Experiments showed that previously initiated shear bands remain active after short interruption without new shear bands nucleated during a compressive test. Reversed shear deformation was also observed along the same slip bands where the previous deformation occurred (Pampillo, 1975). All these observations suggest that BMGs, unlike crystalline metals which are always accompanied with a strain hardening, are inherently *softened* during plastic deformation. In addition, it was found that the deformed region in BMGs was more preferentially etched, and this etching sensitivity would disappear if the glass is heat-treated for certain time (Pampillo, 1975). The formation of nanocrystals within or around shear bands has also been reported in many experiments (Chen et al., 1994; Kim et al., 2002). Those may imply that the softening is fundamentally related to the atomic structure of MG rather than just adiabatic heating which can also give rise to shear localization in some crystalline materials (Rogers, 1979).

Actually there are some previous works considering the important effect of the softening on the development of shear band. By taking free volume as the order parameter, Spaepen proposed a softening mechanism in which an increase of the average free volume within some band will lower the viscosity and thus soften the local material (Spaepen, 1977). This softening mechanism was later examined by Steif et al. (1982) in a one-dimensional numerical analysis with the introduction of an initial perturbation in the average free volume. Argon did similar analysis by introducing a perturbation in strain rate (Argon, 1979). In a recent pinning/depinning model (Vandembroucq and Roux, 2011), the softening/aging in MGs was considered by explicitly shifting the local yield stress threshold after local transformation and the local plastic strain was assumed to obey the same symmetry as the external loading.

Here we propose a *generation-dependent* softening of which the basic physics can be illustrated as in Fig. 3. The idea is that for certain generation change $g \to g + 1$, the Helmholtz free energy change in Eq. (12) can be modified as

$$\Delta F^*_{g \to g+1} = \Delta F_* \exp(-\eta_g), \tag{13}$$

where ΔF_*, as discussed before, is taken as a constant serving as a prefactor, and η_g is a scalar field to represent the amount of local softening at generation g. Apparently $\eta_0 = 0$ applies to every element, assuming the initial system is homogeneously relaxed during processing. As the generation change goes on, η_g will generally increase due to local softening either through the accumulation of "free volume" (Spaepen, 1977) or local heating. Correspondingly the biased activation energy barrier for STZ mode $\epsilon_{ij}^{(m)}$ should be
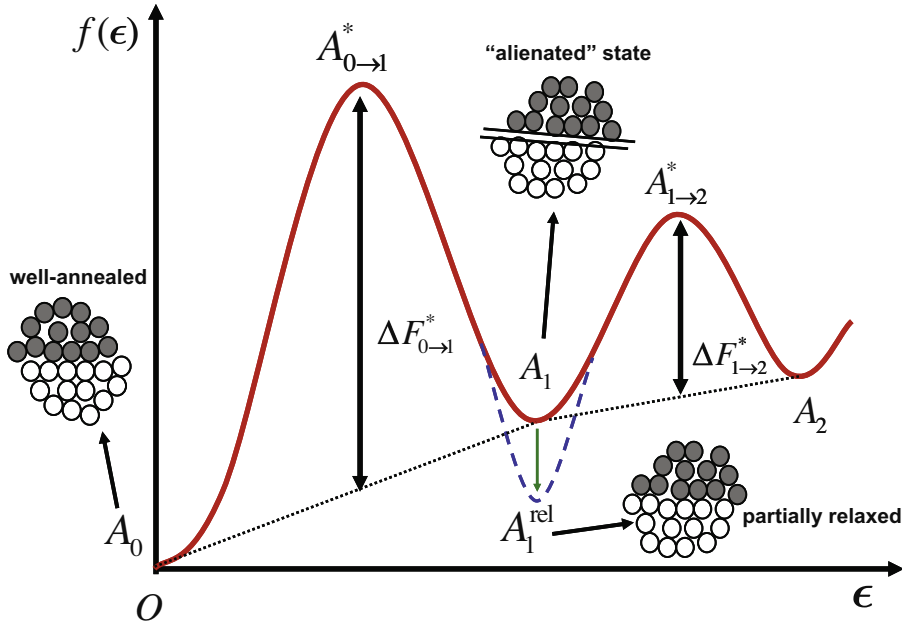
Fig. 3. Energy schematics of softening and partial recovery. Horizontal axis is an "effective" transformation strain during generation changes. For the first generation change $0 \to 1$ occurred at a location labeled A, a saddle point $A_{0\to1}^*$ with energy barrier $\Delta F_{0\to1}^*$ must be overcome. At A_1 before a second transformation occurs, relaxation will bring the system to a lower state A_1^{rel}. However, the system will never reach to a state with the same energy as the initial one, indicating some permanent softening. For the transformation of next generation change $1 \to 2$, the energy barrier $\Delta F_{1\to2}^*$ corresponding to the saddle point $A_{1\to2}^*$ is lowered due to softening.

$$Q^{(m)} = \Delta F_* \exp(-\eta_g) - \frac{1}{2} V_g \sigma_{ij} \epsilon_{ij}^{(m)}. \tag{14}$$

In addition we do not expect local softening will change the local stability of current configuration. That is to say, when the stress bias is zero, the activation energy barrier is still a finite positive value, indicating that the system, although softened, is still in a local minimum so long as there is no applied stress. This suggests that we must put an upper bound η_{max} on the value of η_g. The exact value of η_{max} is related to the maximum free energy change due to the actual softening mechanism. In our simulations, for a parametric study, we set

$$\frac{\Delta F_g^*}{\Delta F_*} = 0.8, \quad \eta_{\text{max}} = -\ln 0.8. \tag{15}$$

Apart from local softening, a partial recovery process is also incorporated based on the work of Dubach et al. (2007). Their fitting of experiment data showed that there is a constant energy barrier Q^{act} to activate a diffusional relaxation process. The corresponding characteristic relaxation time can then be defined as

$$\tau = \frac{1}{v_0 \exp(-Q^{\text{act}}/k_B T)} \tag{16}$$

where v_0 is the atomic vibration frequency on the order of Debye frequency. A lower temperature gives a much larger relaxation time, indicating that the recovery process will be much slower, and vice versa. Then we can separate the softening into two parts:

$$\eta_g = \eta_g^p + \eta^t \exp\left(-\frac{t_{\text{elap}}}{\tau}\right) \tag{17}$$

where η_g^p represents the *permanent* softening that cannot be recovered and η_t is the *temporary* softening that could be recovered through the above diffusional relaxation, and t_{elap} is the time elapsed since the last transformation at the same location. For an initially well relaxed MG sample, there must be $t_{\text{elap}}(\mathbf{x}) \gg \tau$.

To physically account for the softening, the values of η_g^p and η^t need to be formulated based on the amount of transformation that one element has experienced. Define the Von Mises strain invariant of each SFTS tensor as

$$\epsilon^{\text{Mises}} = \sqrt{\epsilon_{23}^2 + \epsilon_{31}^2 + \epsilon_{12}^2 + \frac{(\epsilon_{22} - \epsilon_{33})^2 + (\epsilon_{33} - \epsilon_{11})^2 + (\epsilon_{11} - \epsilon_{22})^2}{6}}, \tag{18}$$

the following linear relations are then formulated to quantitatively describe the softening and partial recovery process:

$$\eta_{g+1}^p = \eta_g^p + \kappa_p(\epsilon^{\text{Mises}})^2, \tag{19}$$

$$\eta^t = \kappa_t(\epsilon^{\text{Mises}})^2. \tag{20}$$

Note that η^p has the generation-dependent accumulative effect due to its permanent nature. On the contrary the effect of η^t is limited to only one generation period, meaning that after each transformation, η^t is recalculated through the new SFTS tensor ϵ and t_{elap} is counted from the start again. The two constants κ_p and κ_t, for the current parametric study, serve only as numerical coefficients. Taking the value of characteristic STZ shear $\gamma_* = 0.1$ and $(\epsilon^{\text{Mises}})^2 = 2*(\gamma_*/2)^2$, the proportional coefficient relating the softening and strain is estimated to be ~40, which should be considered as the total contribution from permanent and temporary softening. Obviously additional assumptions or models are needed to partition between κ_p and κ_t. This could either be obtained form atomistic studies on the softening in MGs, or through fitting the simulation results to experimental data such as yield stress. Here, however, an arbitrary ratio $\kappa_t/\kappa_p = 3$ is assigned for an empirical parametric study. In fact, this ratio could also depend on temperature, since at sufficiently high temperature the significantly increased atomic mobility should relax out all structurally induced softening.

Another important feature that needs to be addressed is the direction-dependence of the local softening. Tests of mechanical creep have confirmed a deformation induced structural anisotropy and a so-called bond-exchange mechanism was proposed to explain this observation (Suzuki et al., 1987). Combining bond-exchange mechanism (Suzuki et al., 1987) with STZ concept, a directional softening scheme may be schematically illustrated as in Fig. 4. It should be pointed out that different atomic configurations are very likely to give rise to different directionalities of softening, and the main purpose of Fig. 4 is to suggest that the STZ transformation, like dislocation slip in crystals, could have some "preferred" directions, especially when the short/medium-range ordering (Hirata et al., 2011) is considered. This can also be seen from Fig. 3 where at generation-1 the energy barrier for the next generation change, e.g. $A_1 \rightarrow A_0$ or $A_1 \rightarrow A_2$, is obviously different depending on the *direction* of the transformation. In fact Fig. 3 already assumes the second transformation is described by the same reaction coordinate, implying the "direction" can only be either the same or the opposite. In the actual energy landscape the reaction coordinate for the next STZ transformation could be more complicated. To capture the directional feature of softening, the scalar order parameter η_g is obviously not sufficient. Thus we introduce another generation-dependent order parameter, $\xi^{(m)}$, a *direction factor* defined as

$$\zeta_g^{(m)} = \frac{\boldsymbol{\varepsilon}_{g-1} \cdot \boldsymbol{\epsilon}_g^{(m)}}{\|\boldsymbol{\varepsilon}_{g-1}\| \cdot \|\boldsymbol{\epsilon}_g^{(m)}\|}, \quad m = 1, 2, \ldots, \mathcal{M} \tag{21}$$

where the strain is in the following vector representation

$$\boldsymbol{\varepsilon} = (\varepsilon_{11}, \varepsilon_{22}, \varepsilon_{33}, \sqrt{2}\varepsilon_{23}, \sqrt{2}\varepsilon_{13}, \sqrt{2}\varepsilon_{12})^T. \tag{22}$$

ξ then represents the direction of one STZ mode with respect to previous actual transformation. The maximum $\xi = 1$ means it continues to transform along the previous direction, and the complete opposite for the minimum $\xi = -1$. A directional softening requires that there is a distribution of η with respect to ξ, or we can write the total softening as a function of $\xi \in [-1, +1]$:

$$\eta_g(\xi) = P(\xi)\eta_g \tag{23}$$

where η_g is calculated by current state variables according to Eq. (17) and Eq.(19), and $P(\xi)$ is a certain distribution. Falk and Langer developed a STZ theory based on an assumption that STZ is a two-state entity which can only transform either forward or backward (Falk and Langer, 1998), suggesting an extreme directional feature. However there is no experimental evidence for such two-state assumption (Takeuchi and Edagawa, 2011). The exact form of $P(\xi)$ could be very complex, and since we are only interested in the average behavior, four simple distributions are proposed in Fig. 5 for a parametric study. Although ξ represents the *relative* direction between the accumulated transformation strain and the potential transition path, one may still argue that, for a specific scheme as in Fig. 5, the softening could be biased in a particular direction. How-
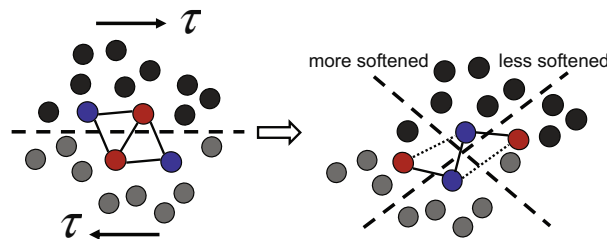
Fig. 4. The bond-exchange mechanism (Suzuki et al., 1987) is used to schematically illustrate the directional softening. At the transformed (softened) state, the bonding conditions is expected to be different along different directions.

ever, because of the heterogeneous catalogs for STZs, this correlation of directionality will quickly be disturbed and eliminated within several generations due to the long-range elastic interaction. In fact, there is always a "back stress" from the matrix, driving the inclusion to transform back, and its competition with softening directionality is very likely to produce a *statistically* isotropic softening, rendering the directionality as a *secondary* effect. This will be further discussed later.

2.2. Transformation elasticity

The actual strain and stress field after a transformation are obtained by solving the following equations:

$$F_{el}[\mathbf{H}, \boldsymbol{\epsilon}(\mathbf{x})] \equiv \min_{\mathbf{u}(\mathbf{x})} F_{el}[\mathbf{u}(\mathbf{x})|\mathbf{H}, \boldsymbol{\epsilon}(\mathbf{x})] \tag{24}$$

$$F_{el}[\mathbf{u}(\mathbf{x})|\mathbf{H}, \boldsymbol{\epsilon}(\mathbf{x})] \equiv \frac{1}{2} \int d^3\mathbf{x} \, c_{ijpq}(\mathbf{x})(\varepsilon_{ij}(\mathbf{x}) - \epsilon_{ij}(\mathbf{x}))(\varepsilon_{pq}(\mathbf{x}) - \epsilon_{pq}(\mathbf{x})) \tag{25}$$

where $\mathbf{u}(\mathbf{x}) \equiv \mathbf{x}' - \mathbf{x}$ is the difference between the new position $\mathbf{x}'$ and the old position $\mathbf{x}$, and is related to the actual transformation strain

$$\varepsilon_{ij}(\mathbf{x}) \equiv \frac{u_{i,j} + u_{j,i}}{2}. \tag{26}$$

$\mathbf{H}$ is the new supercell matrix (three supercell edge vectors being the row vectors of the matrix) which is related to the original supercell $\mathbf{H}_0$ by $\mathbf{H} = \mathbf{H}_0(\mathbf{I} + \bar{\boldsymbol{\varepsilon}})$, with $\bar{\boldsymbol{\varepsilon}}$ the overall average strain of the supercell. Because of periodic boundary condition, there must be

$$\mathbf{u}(\mathbf{x} + \mathbf{h}_0) - \mathbf{u}(\mathbf{x}) = \mathbf{h}_0 \bar{\boldsymbol{\epsilon}} \tag{27}$$

where $\mathbf{h}_0$ is one of the $\mathbf{H}_0$ edge vectors. So

$$\int_0^{\mathbf{h}_0} d\mathbf{x}' \cdot \frac{d\mathbf{u}(\mathbf{x} + \mathbf{x}')}{d\mathbf{x}'} = \mathbf{h}_0 \bar{\boldsymbol{\epsilon}} \rightarrow \int d^3\mathbf{x} \frac{d\mathbf{u}}{d\mathbf{x}} = \det|\mathbf{H}_0| \bar{\boldsymbol{\epsilon}}. \tag{28}$$

Note that, because of Eq. (26), $\{\varepsilon_{ij}(\mathbf{x})\}$ need to satisfy compatibility constraints

$$\varepsilon_{ii,jj} + \varepsilon_{jj,ii} = 2\varepsilon_{ij,ij}, \quad \forall i \neq j \tag{29}$$

which means the $\{\varepsilon_{ij}(\mathbf{x})\}$ fields are not independent fields in the variational functional (the $\{u_i(\mathbf{x})\}$ fields are). On the other hand, there is no compatibility constraint on the stress-free strain fields $\{\epsilon_{ij}(\mathbf{x})\}$, which are "given" in the elastic constant minimization problem.

The functional to be minimized in Eq. (25) represents a quadratic expansion approximation of the Helmholtz free energy (Li, 2000) around the *freely transformed* block. Unlike the more general nonlinear formulation and minimization, the merit of the quadratic expansion is that Eq. (25) is quadratic in $\mathbf{u}(\mathbf{x})$, whose minimization (in principle at least) entertains a close-formed solution in the form of a matrix inverse, after real-space discretization of $\mathbf{u}(\mathbf{x})$ and representation
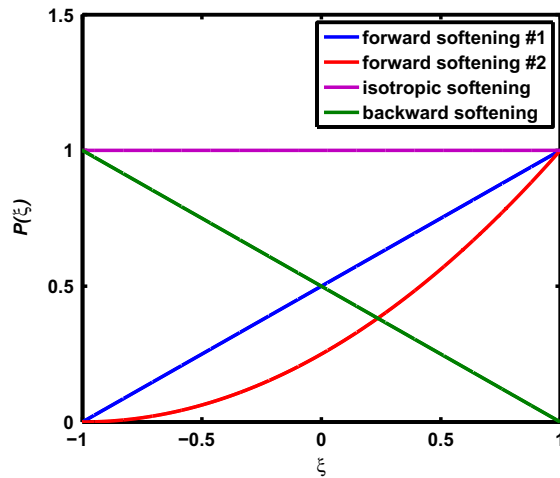
Fig. 5. Different schemes for distributions of $P(\xi)$ ($\xi \in [-1, 1]$). Forward softening scheme 1: $P(\xi) = \frac{1}{2}(1 + \xi)$; forward softening scheme 2: $P(\xi) = \frac{1}{4}(1 + \xi)^2$; isotropic softening: $P(\xi) = 1$; backward softening: $P(\xi) = \frac{1}{2}(1 - \xi)$.

of ∇^2-like operators. We have the stress equilibrium equation in structurally inhomogeneous and elastically inhomogeneous material:

$$(c_{ijpq}(\mathbf{x})(u_{p,q}(\mathbf{x}) - \epsilon_{pq}(\mathbf{x})))_{,j} = 0, \quad \forall i = 1 \ldots 3 \tag{30}$$

In this paper, however, we only consider the elastically homogeneous problem with $c_{ijpq}(\mathbf{x}) = c_{ijpq}$ (for cases like MG-matrix composites (Hofmann et al., 2008) where elastic heterogeneity must be considered, we will adopt the technique proposed in Wang et al. (2002)). Then the problem is simplified into

$$c_{ijpq}(u_{p,q}(\mathbf{x}) - \epsilon_{pq}(\mathbf{x}))_{,j} = 0, \quad \forall i = 1 \ldots 3 \tag{31}$$

and the inverse can be done in the Fourier space on a $\mathbf{k}$-by-$\mathbf{k}$ basis. We first note that $u_p(\mathbf{x})$ can be decomposed into a secularly growing component in $\mathbf{x}$, plus a periodic component:

$$u_p(\mathbf{x}) \equiv \mathbf{x}\bar{\epsilon} + \tilde{u}_p(\mathbf{x}) \tag{32}$$

Then stress equilibrium requires that in $\mathbf{k}$-space:

$$-c_{ijpq}k_q k_j \tilde{u}_p(\mathbf{k}) = ic_{ijpq}\epsilon_{pq}(\mathbf{k})k_j \tag{33}$$

where

$$\tilde{u}_p(\mathbf{k}) \equiv \int d^3\mathbf{x}\tilde{u}_p(\mathbf{x})e^{-i\mathbf{k}\cdot\mathbf{x}}, \quad \tilde{u}_p(\mathbf{x}) = \frac{1}{\det|\mathbf{H}_0|}\sum_{\mathbf{k}}\tilde{u}_p(\mathbf{k})e^{i\mathbf{k}\cdot\mathbf{x}}, \tag{34}$$

and similarly $\epsilon_{pq}(\mathbf{k}) \leftrightarrow \epsilon_{pq}(\mathbf{x})$. Eq. (33) is also used by Khachaturyan (1983) in deriving a close form of the coherency strain energy for an arbitrary coherent multi-phase alloy. If we define symmetric matrix $\mathbf{C}(\hat{\mathbf{k}})$ (Wang et al., 2002)

$$C_{ip}(\hat{\mathbf{k}}) \equiv c_{ijpq}\hat{k}_q\hat{k}_j, \quad \hat{\mathbf{k}} \equiv \frac{\mathbf{k}}{|\mathbf{k}|}, \tag{35}$$

the inverse matrix is also real and symmetric: $\Omega(\hat{\mathbf{k}}) \equiv \mathbf{C}^{-1}(\hat{\mathbf{k}})$. Let us also define strain-free stress:

$$\sigma_{ij}^0(\mathbf{x}) \equiv c_{ijpq}\epsilon_{pq}(\mathbf{x}), \quad \sigma_{ij}^0(\mathbf{k}) \equiv c_{ijpq}\epsilon_{pq}(\mathbf{k}), \tag{36}$$

then

$$-|\mathbf{k}|^2 C_{ip}(\hat{\mathbf{k}})\tilde{u}_p(\mathbf{k}) = i\sigma_{ij}^0(\mathbf{k})k_j \tag{37}$$

and $\tilde{u}_p(\mathbf{k})$ is obtained explicitly as

$$\tilde{u}_p(\mathbf{k}) = \frac{\Omega_{pi'}(\hat{\mathbf{k}})\sigma_{i'j'}^0(\mathbf{k})k_{j'}}{i|\mathbf{k}|^2}. \tag{38}$$

Since $i\sigma_{ij}^0(\mathbf{k})k_j$ represents the divergence of stress, or net force, $-\frac{\Omega_{pi}(\hat{\mathbf{k}})}{|\mathbf{k}|^2}$ is just the infinite-space Green's function relating force to displacement in this translationally invariant system. This Green's function is short-ranged in reciprocal space (in fact $\mathbf{k}$-by-$\mathbf{k}$ local), but long-ranged in real space. Thus it is advantageous to solve homogeneous-material problems in reciprocal space, which is more generally called the spectral method.

The strain field that corresponds to the Eq. (38) displacement field is

$$\tilde{\epsilon}_{pq}(\mathbf{k}) = \frac{ik_q\tilde{u}_p(\mathbf{k}) + ik_p\tilde{u}_q(\mathbf{k})}{2} = \frac{\Omega_{pi'}(\hat{\mathbf{k}})\sigma_{i'j'}^0(\mathbf{k})\hat{k}_{j'}\hat{k}_q + \Omega_{qi'}(\hat{\mathbf{k}})\sigma_{i'j'}^0(\mathbf{k})\hat{k}_{j'}\hat{k}_p}{2}, \tag{39}$$

$$\epsilon_{pq}(\mathbf{x}) = \bar{\epsilon}_{pq} + \tilde{\epsilon}_{pq}(\mathbf{x}), \quad \int d^3\mathbf{x}\tilde{\epsilon}_{pq}(\mathbf{x}) = 0. \tag{40}$$

For 2D isotropic medium, we have

$$c_{ijpq} = \lambda\delta_{ij}\delta_{pq} + \mu(\delta_{ip}\delta_{jq} + \delta_{iq}\delta_{jp}). \tag{41}$$

Plug this into the strain-free stress and we will get the specific expression for the strain field, and hence the stress field. More detail is presented in Appendix C.

2.3. Time evolution

We use a computational supercell of $N \times N$ voxels under periodic boundary condition. Each element is available for $\mathcal{M}$ different STZ transformation modes with SFTS tensors $\epsilon^{(m)}$. The state configuration at generation-g, labeled as $\mathbf{S}_g(\mathbf{x})$, is then completely described as

$$\mathbf{S}_g(\mathbf{x}) \leftarrow \{\boldsymbol{\epsilon}(\mathbf{x}), \boldsymbol{\sigma}(\mathbf{x}), \eta_{\mathbf{g}}^{\mathbf{p}}(\mathbf{x}), \eta^{\mathbf{t}}(\mathbf{x}), t_{\mathbf{elap}}(\mathbf{x})\}. \tag{42}$$

Since the dynamics is biased by thermal fluctuation, load-shedding elastic interactions, and generation-dependent softening, different elements may eventually stay at different generations.

Simulations on uniaxial tensile tests under strain-controlled condition are performed in this paper. Given the applied strain rate $\dot{\bar{\varepsilon}}$ and strain increment $\Delta\bar{\varepsilon}$ at each simulation step, there is a time interval $\Delta t = \Delta\bar{\varepsilon}/\dot{\bar{\varepsilon}}$ which is the maximum residence time the system can stay at current configuration. During Δt the applied stress may drive the system to three different responses: athermal plasticity, thermal plasticity, and pure elasticity.

1. If stress field $\boldsymbol{\sigma}(\mathbf{x})$ is sufficiently high, the current configuration may not be stable anymore with some biased activation energy barrier being negative. We transform simultaneously all the elements with a negative energy barrier along the corresponding path. If one element has two or more such paths, we choose the one with the lowest energy barrier.
2. If the calculated $\mathcal{M} \times N \times N$ barriers are all positive, STZ transformations are considered as *thermally* activated events. The resulted "state-to-state" dynamics is simulated using kMC algorithm. The rate catalog consisting of $\mathcal{M} \times N \times N$ transition states is determined as

$$k_i^{(m)} = v_0 \exp(-Q_i^{(m)}/k_{\mathrm{B}}T), \quad m = 1, 2, \ldots, \mathcal{M}, \tag{43}$$

where $i = 1, 2, \ldots, N \times N$ represents different elements. The residence time is then on average given by Voter (2007)

$$t_{\mathrm{res}} = 1 \Big/ \sum_{i,m} k_i^{(m)}. \tag{44}$$

Thermal plasticity has probability $1 - \exp(-\Delta t/t_{\mathrm{res}})$ to occur in the time interval. To model this, we take a uniformly distributed random variable $\eta \in (0, 1]$, and check
   (a) If $\eta > \exp(-\Delta t/t_{\mathrm{res}})$, thermal plasticity will occur. If that is the case we can use standard kMC algorithm to select one transition state using a random number ζ uniformly distributed on $(0, 1]$. For the convenience of implementation, we replace the indexing of rate constants with k_j, $j = 1, \ldots, n_{\mathrm{tot}}$ with $n_{\mathrm{tot}} = \mathcal{M} \times N \times N$. Then we can calculate cumulative sums

$$q_i = \sum_{j=1}^{i} k_j, \quad i = 1, \ldots, n_{\mathrm{tot}}. \tag{45}$$

Then the selected transition state has the index s satisfying

$$q_{s-1} < \frac{\zeta}{t_{\mathrm{res}}} \leqslant q_s. \tag{46}$$

   (b) If $\eta \leqslant \exp(-\Delta t/t_{\mathrm{res}})$, it is assumed that the thermal plasticity cannot be activated before the next applied strain, and the system is simply elastically deformed during Δt.

A somewhat detailed issue is with racing and the stress value used in the time-stepping. Since voxel stress $\boldsymbol{\sigma}^{i,j}$, where i,j index the 2D position of a voxel, influences the activation energy inside an exponential, the voxel transition rates could be quite sensitive functions of $\boldsymbol{\sigma}^{i,j}$. In principle, using both $\boldsymbol{\sigma}^{i,j}(t)$ (Forward Euler) and $\boldsymbol{\sigma}^{i,j}(t + \Delta t)$ (Backward Euler) should be equally valid and accurate (first-order methods) for computing the $t \to t + \Delta t$ transition rate, but of course using the latter for implicit integration will be computationally more expensive, without improving the accuracy of time-stepping. A time-adjustment procedure could be worked out that effectively uses $(\boldsymbol{\sigma}^{i,j}(t) + \boldsymbol{\sigma}^{i,j}(t + \Delta t))/2$ for second-order time integration, if one maintains the same transition event regardless of stress value. If the rates of multiple transition events vary a lot from $\boldsymbol{\sigma}^{i,j}(t)$ to $\boldsymbol{\sigma}^{i,j}(t + \Delta t)$, then racing could happen, and to achieve second-order accuracy, one must do iterations.

3. Results and discussion

To demonstrate the capability of our model, simulations on uniaxial tensile test are carried out to study the formation of shear bands. In order to see the effect of softening, we analyze the extreme value statistics during deformation. The local temperature rise is also estimated as well.

A plate geometry with periodic boundary condition is used, implying a 2D simulation with plane-stress constraint. Each element is assigned to be 1.7 nm $\times$ 1.7 nm, which agrees with typical STZ size (Johnson and Samwer, 2005; Mayr, 2006; Pan et al., 2008). Material properties are listed in Table 1, adopted from typical MG systems in the literature. The γ_* in Table 1, the characteristic shear of STZ (Argon and Shi, 1983; Schuh et al., 2007), is used to scale the numerically generated SFTS components.

Table 1
List of simulation parameters.

Parameter	Value
E	88.6 GPa (Bian et al., 2002)
v	0.371 (Bian et al., 2002)
v_0	1×10^{13} Hz
ΔF_*	5 eV
Q_{act}	0.37 eV (Dubach et al., 2007)
κ_p	10
κ_t	30
γ_*	0.1 (Argon and Shi, 1983; Schuh et al., 2007)
T	300 K
$\dot{\bar{\varepsilon}}$	1×10^{-4} s^{-1}
$\Delta \bar{\varepsilon}$	1×10^{-4}

3.1. Parametric study I: number of STZ modes

Simulation results with the same system size of 217.6 nm × 217.6 nm but different number of STZ modes, $\mathcal{M}$, are presented in Fig. 6. Note that since there is no decohesion or fracture mechanisms in our model, plastic deformation continues after the load drop. Let us focus on the stress–strain curves at small strains within the ductility of typical monolithic MGs. It is shown clearly that large $\mathcal{M}$ produces a stress drop at the upper yielding point, which corresponds to the nucleation of shear band indicated by plotting the distribution of the Von Mises strain invariant of transformation strain as shown in Fig. 7. When $\mathcal{M}$ is small, the system is more "frustrated" to find a mode that is in alignment with the "favored" mode defined by the elastic interaction and served as a *kernel* for the shear band. The fewer the possible modes are, i.e., the smaller the $\mathcal{M}$ is, the more the system is "frustrated", resulting in a delay in the formation of a shear band as shown in Fig. 7. This is consistent with the limit case of $\mathcal{M} \to \infty$ we discussed in Section 2.1.2. The dash line in Fig. 6 represents the stress–strain curve obtained from a simulation with $\mathcal{M} = 12$ but $\Delta F_* = 4.5$ eV. There is no stress drop, but the flow stress is lowered to approximately the same level as the case of $\mathcal{M} = 20$. The difference, however, is that after about 6% applied strain, the case $\mathcal{M} = 12$ ($\Delta F_* = 4.5$ eV) shows a "strain-hardening", while the case $\mathcal{M} = 20$ still displays a steady flow in average.

$\mathcal{M}$ is essentially a topological parameter of the energy landscape of MG (Li et al., 2011), and is likely quite system- and processing-dependent. For the same glass chemistry, a faster cooling history or a stress-induced rejuvenation (Takeuchi and Edagawa, 2011) would imply a higher energy state for the processed MG and correspondingly a lower stress-free activation barrier for STZ transformation. This also means that $\mathcal{M}$ in reality is related to other activation parameters and independent variation of $\mathcal{M}$ while keeping all the other activation parameters fixed, like that shown in Fig. 6, is just a theoretical exercise. In view of this, assuming a constant $\mathcal{M}$ for all generations, though convenient, is also likely to introduce errors, since stress-rejuvenated state could be more connected and has lower barriers (Sciortino et al., 1999; Kushima et al., 2009; Li et al., 2011). This error will be investigated in later models (Zhao et al., submitted for publication).

The obtained stress–strain curves in Fig. 6 are similar to the study by Utz et al. on stress–strain curves for model MGs produced by different quenching rates (Utz et al., 2000), where the obtained systems are at different energy states. In the
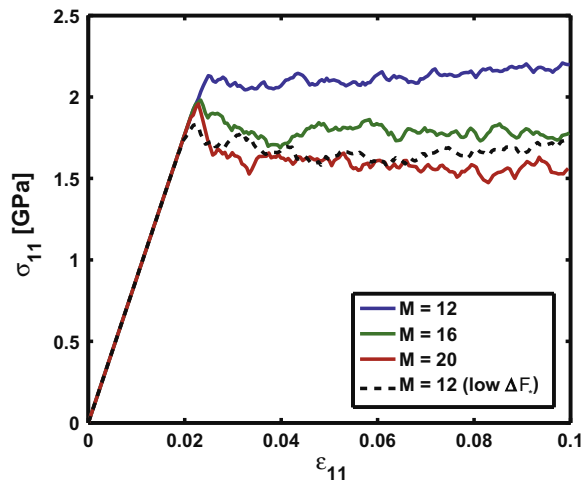
Fig. 6. Stress–strain curves with number of STZ modes being 12, 16, and 20. The dash line represents same simulation with 12 modes but a lower stress-free activation energy barrier for STZ.
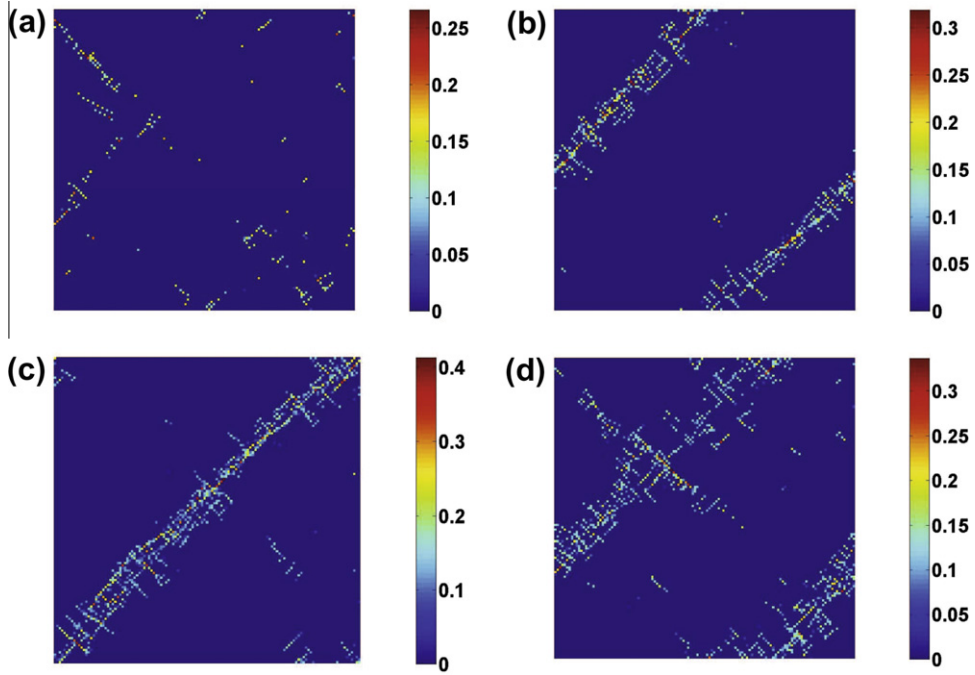
Fig. 7. Transformation strain distributions after 2.5% applied strain for simulations with (a) $\mathcal{M} = 12$, (b) $\mathcal{M} = 16$, (c) $\mathcal{M} = 20$, and (d) $\mathcal{M} = 12$ (low ΔF_*), corresponding to different stress–strain curves shown in Fig. 6.

following simulations we set $\mathcal{M} = 20$, which for the given $\Delta F_* = 5$ eV could represent a well annealed MG based on the comparison with MD simulations, in order to study the formation of shear band in MG.

3.2. Parametric study II: directional softening

Simulations with 4 different $P(\xi)$ are shown in Fig. 8 and the one without softening is presented as dash line for reference. As we expected, the backward softening $P(\xi) = \frac{1-\xi}{2}$ gives the highest yield point, since the preferential softening direction will always tend to erase the previous softening effect by promoting an opposite transformation. The isotropic softening $P(\xi) = 1$ gives no yield strength decrease. Both forward softening schemes result in an overall softening with obvious yield point drops. These are consistent with the energetics shown in Fig. 3. In the following we use $P(\xi) = \frac{(1+\xi)^2}{4}$ as our directional softening scheme to study shear band formation. It should be pointed out that, although the isotropic softening gives no
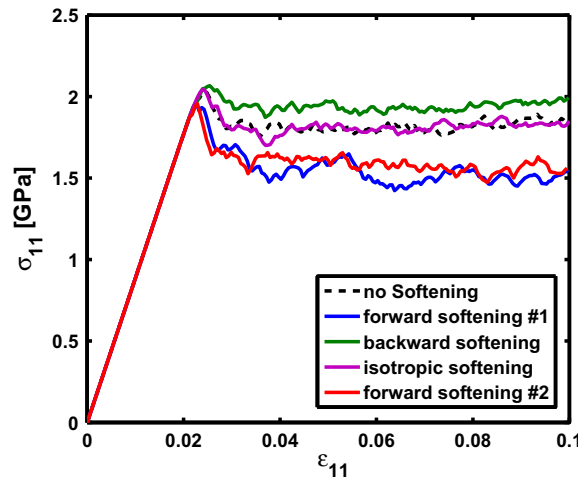

Fig. 8. Stress–strain curves with four different $P(\xi)$ in Fig. 5. The dash line is for the simulation without softening.

yield strength decrease, it can still localize the strain and lead to shear band formation. This actually confirms our expectation that the directionality of softening is statistically equivalent to an isotropic scheme and is therefore a secondary effect.
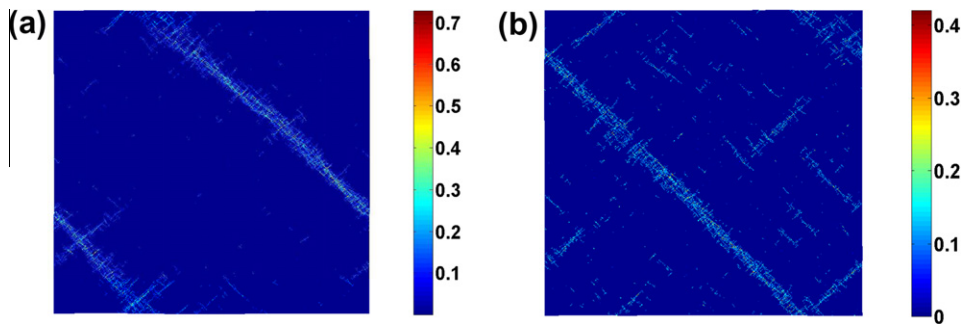
3.3. Shear band formation

The typical shear localization at room temperature is observed in our tensile test simulations. Results obtained for a system of 512×512 voxels (i.e. 870.4 nm $\times$ 870.4 nm) are shown in Fig. 9 (left column). For comparison, results obtained for an identical system but without softening are also shown in Fig. 9 (right column). It is clear that localized deformation, i.e. shear band formation occurs only when softening is considered. Without softening the deformation is homogeneous even though the deformation appears to be localized at the early stage when the yield (the drop on stress–strain curve) just occurs (Fig. 10(b)). The "yield strength", i.e. the peak stress and the steady flow stress are both lowered for the case with softening, which is what we expected from the softening term introduced in our model.

The transformation strain distributions after the system undergoes an average strain of 2.5% are shown for both simulations in Fig. 10 for both cases. It seems that nucleation of shear bands can still be present in the absence of softening,
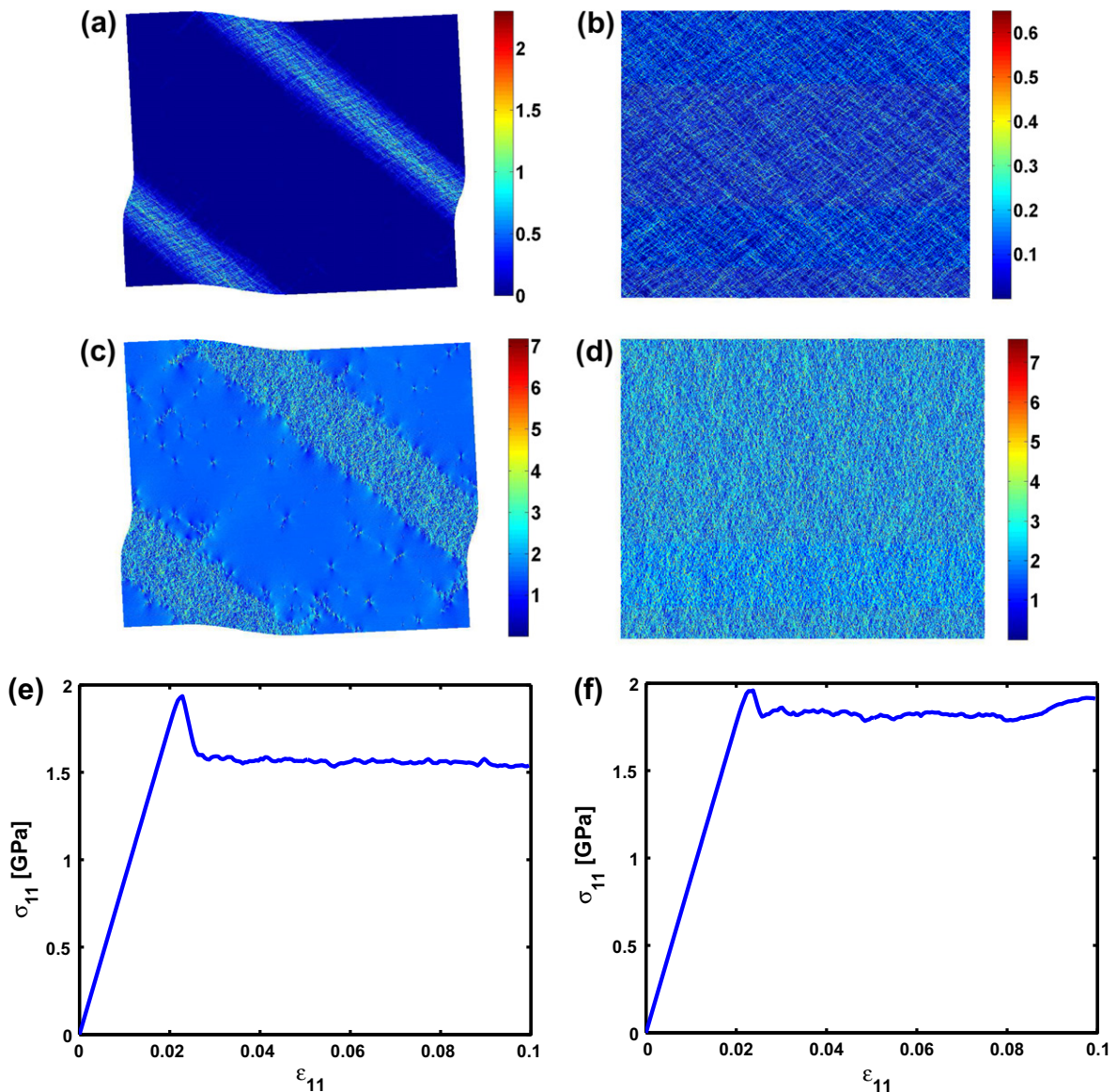
Fig. 9. Deformation behavior in a system of 870.4nm $\times$ 870.4nm, with (left column) and without (right column) softening. (a) and (b) Distributions of Von Mises strain of the transformation strain tensor; (c) and (d) distributions of equivalent Von Mises stress (the unit for colorbar is GPa); (e) and (f) stress–strain curves.

Fig. 10. Transformation strain distribution right after the nucleations of shear bands in simulations (a) with and (b) without softening incorporated.

suggesting that the nature of shear band nucleation could essentially be a collective motion of multiple STZs due to load-shedding elastic interactions between elements. This is similar to the idea behind the yielding criterion proposed by Packard and Schuh (2007) where the shear path in MGs is controlled by a certain plane along which a critical strength value is exceeded everywhere, rather than by some local point with an overall maximum shear. Such plane criterion in amorphous alloys may only be satisfied by certain stress field configuration rather than forming actual "lattice planes".

On the other hand, the stress field caused by STZ transformations alone, cannot localize the accommodation of further shear strain. Without softening, the initially formed shear band will spread over the entire system. This corresponds to the state with an average strain of about 8% in Fig. 9(f), followed with a "strain-hardening". The reason for such shear band thickening is that, in the absence of softening, there is no internal structural difference between the transformed and untransformed regions and the only inhomogeneity is due to the local stress field. Thus the merit of generation-dependent softening is to take into account of the structural heterogeneity introduced in generation changes during deformation. Unlike the analysis of Steif et al. (1982) and Argon (1979) in which geometric heterogeneity was assumed, our initial "glass" is structurally homogeneous as in real glasses. This softening-controlled shear band growth may also explain why Homer et al. cannot observe shear localization for a well relaxed MG (Homer and Schuh, 2009), since there is no softening mechanism in their model.

As a basic characteristics, the thickness of shear bands has been measured extensively by experiments, suggesting a value of ∼10 nm (Zhang and Greer, 2006). In our simulations, even in the presence of softening, the shear band will grow in width as the applied elongation continues because no fracture is considered in the model. Considering the fact that experimental measurements are usually corresponding to shear bands at fracture (less than ∼3% elongation), we thus report here the simulated shear band thickness at the applied strain of both 2.5% and 10% as shown in Fig. 11, where the results for different computational supercell sizes are presented. While the thickness of the shear bands right after nucleation (2.5% strain) is independent of supercell size and in average gives a value of 18.5 nm, a size-dependence clearly arises after a period time of continued elongation (10% strain). The discussion on the system size effect will be detailed in the following section.

3.4. Extreme value statistics

While the mean and variance of a distribution are often used to characterize a statistical distribution, these moments reflect population averages that sometime obscure the so-called extreme value (EV) (Fisher and Tippett, 1928; Pickands, 1975;
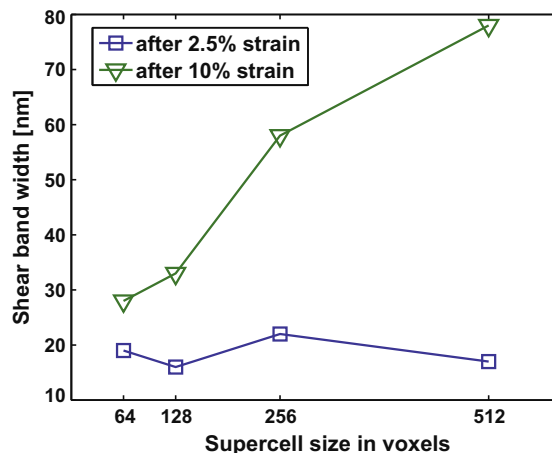
Fig. 11. The thickness of shear bands at the applied strain of 2.5% (square) and 10% (triangle) respectively for different simulation sizes.

Reiss and Thomas, 2007) information, which is concerned with the maximal and minimal values in a statistical sample. The importance of EV can be appreciated by considering, for instance, the significance of world record in sports, or the importance of Fortune 100 companies in global business. For the failure of metallic glasses, extreme value at the level of STZ is expected to be crucial, since cracking of a single STZ (∼1.7 nm) that have accumulated enough shear strain could initiate decohesion events that lead to the final catastrophic failure of the entire piece (Shimizu et al., 2006, 2007).

Fig. 12 shows the probability density distribution of the Von Mises strain of voxels in the material after 10% applied strain. In both cases (i.e. with and without softening) there is a peak at approximately the same position of around 0.1 Von Mises strain. The main difference is the much longer tail of distribution when softening is considered. The extreme sites corresponding to this long tail are where the most severe inelastic transformation occurs and could be responsible for many interesting observations such as local heating (Lewandowski and Greer, 2006), cavitation and nanovoid formation (Li et al., 2002), which lead to fracture. The evolution of extreme Von Mises strain during the deformation is also presented as the inset in Fig. 12. The softening gives a much more rapid "runaway" behavior of these extreme sites. This may be the reason why most MGs have a very limited ductility.

To explain the position of the peak probability, we continue to elongate the system to 20% applied strain and compare the corresponding probability density with the case of 10% applied strain. The result is shown in Fig. 13. It shows that even after more macroscopic strain is applied, the peak still stays at 0.1 Von Mises strain. This implies the peak is due to the characteristic STZ transformation strain γ_* rather than external applied strain. Again, the major difference lies in the more extended long tail.

As an example to show the role played by these extreme sites, we give a simple estimation on the local temperature rise during the above simulation. For each STZ transformation, the work that is dissipated is given by

$$\Delta W(\mathbf{x}) = V\Delta w(\mathbf{x}) = V\sigma_{ij}(\mathbf{x})\epsilon_{ij}(\mathbf{x}). \tag{47}$$

where Δw is the energy density dissipated due to plastic deformation. Assuming STZ transformation is instantaneous and fully adiabatic, the local temperature rise is simply

$$\Delta T(\mathbf{x}) = \frac{\Delta W(\mathbf{x})}{mC} = \frac{\Delta w(\mathbf{x})}{\rho C} \tag{48}$$

where m is the mass, ρ is the density, and C is the heat capacity. Then the heat conducting equation is

$$\frac{\partial T(\mathbf{x},t)}{\partial t} = \left(\frac{k}{C\rho}\right)\nabla^2 T(\mathbf{x},t) \tag{49a}$$

$$T(\mathbf{x}, t = 0) = T_0(\mathbf{x}) + \Delta T(\mathbf{x}) \tag{49b}$$

where k is the thermal conductivity. For each simulation step with an initial temperature distribution $T_0(\mathbf{x})$, the corresponding initial condition $T(\mathbf{x}, t = 0)$ for the above heat conducting equation is given by adding the instantaneous temperature increase Eq. (48) due to local plastic events, i.e. STZ transformations. The voxel-level temperature propagation equation Eq. (49b) can be solved easily in reciprocal space using Fourier spectral method as in calculating the stress field. We use $\rho = 6125$ kg/m³, $C = 420$ J/(kg · K), and the thermal diffusivity $\alpha = \frac{k}{\rho C} = 3 \times 10^{-6}$ m²/s, which are all taken from Lewandowski and Greer (2006). The result is shown in Fig. 14. As is expected, the "runaway" feature is similar to that in the evolution of
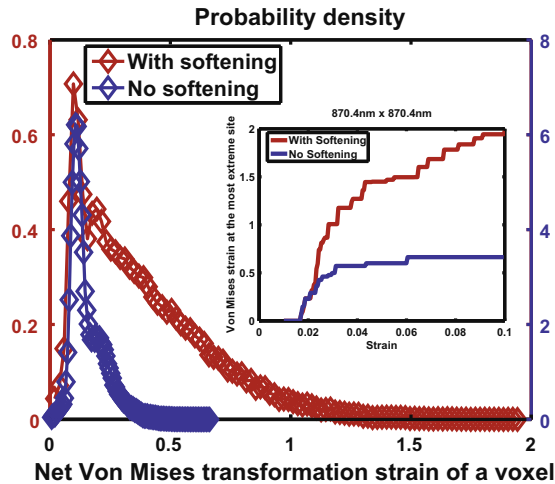

Fig. 12. The probability density distribution of the Von Mises strain invariant of voxels in the material after 10% applied strain as in Fig. 9. The left y-axis is for the case with softening and the right y-axis is for the case without softening. The inset shows how the maximum Von Mises strain changes as the average strain increases.
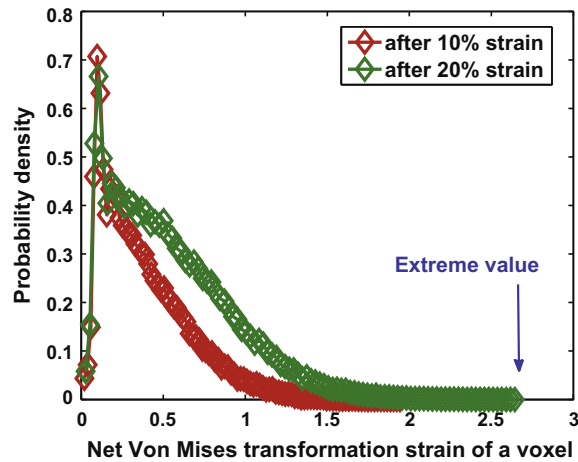
Fig. 13. The probability density distributions of the Von Mises strain of voxels in the material after 10% and 20% applied strain respectively.

maximum Mises strain in the inset of Fig. 12. The softening effect promotes significantly the local temperature rise. In experiments it is chalenging to make a direct and accurate measurement on the instantaneous temperature rise within the nanoscale shear bands. Using an infrared camera, Yang et al. measured a temperature rise ~1K and estimated that the actual value could be as high as 650 K (Yang et al., 2005). In a method based on fusible Sn coating, Lewandowski and Greer (2006) was able to measure a temperature rise of 207 K with better spatial and temporal resolution; and the thin-film solution estimated that the center of the shear band could reach a temperature as high as over 3000 K, which is in agreement with the current work. The combination of local intensive shear and temperature rise is then expected to give rise to a more amplified "autocatalytic" effect and lead to abrupt failure with limited ductility.

3.5. The system size effect

The system size dependence of the evolution of the maximum Von Mises strain is shown in Fig. 15. At the strain of around 2.5%, larger system size gives rise to a more abrupt "runaway" feature. This size-dependence can be understood if we recall that in Fig. 11 the corresponding shear band thickness is independent of the supercell size. Therefore, the shear band corresponding to a smaller volume fraction in a larger system has to accommodate more strain to reach the same level of average applied strain. The reason for the limited thickness of shear band nucleation resides in the fact that the voxel in our model corresponds to the actual physical length (~1.7 nm) of STZ. This yields a stress field which is independent of the computational grid, resulting in an absolute critical size of shear band "embryo". Our simulation in fact also confirms this perspective, for if we inspect the strain distribution as in Fig. 10 at early stage of nucleation, we find frequently a cluster of 7 transformed voxels spreading along one maximum shear direction into a line and shear bands are nucleated by extending along the other
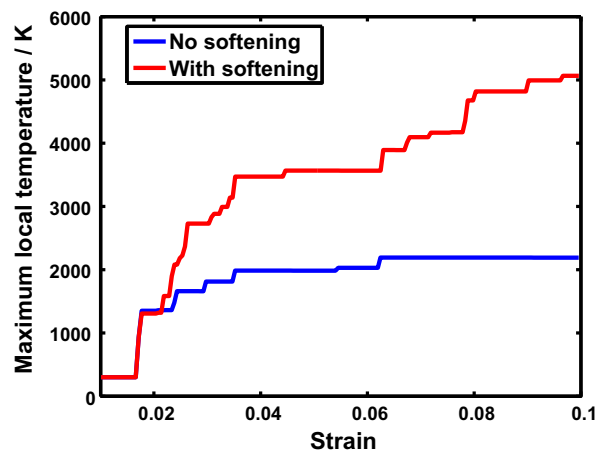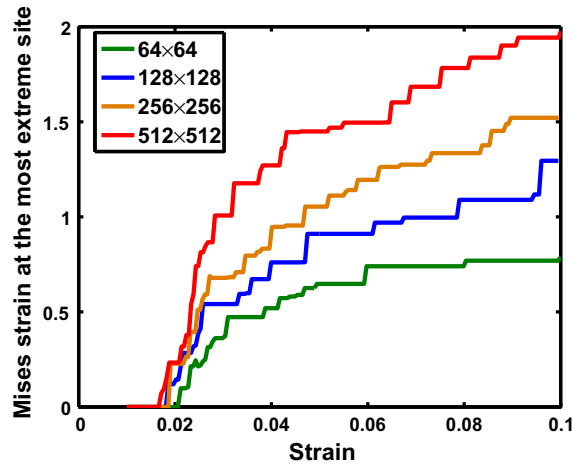

Fig. 14. Evolution of the maximum local temperature at the single-voxel level during the deformation. The "runaway" feature is the same as in the evolution of maximum von Mises strain.

Fig. 15. Size effect on the maximum Von Mises strain evolution during deformation. The supercell size is indicated and can be converted to physical size by multiplying the length of STZ (~1.7 nm).

maximum shear direction. Such cluster corresponds to a characteristic length ~17 nm, which is indeed consistent with our measurement.

On the other hand, the size-dependent thickness of shear bands after 10% applied strain as shown in Fig. 11 may put the statistics in Fig. 15 into question, since the increased volume fraction of shear bands may lead to the appearance of more extreme values. However, inspection on extreme values (long tails in Fig. 13) reveals that the corresponding sites are all located in the center of the shear bands, rather than uniformly distributed, confirming no statistical artifact on the size-dependence of maximum Von Mises strain. In fact those extreme sites after even 10% strain are inherited from previous generations when the shear band is newly nucleated, and eventually form the "core" (hot) region, of which the extent is again controlled by the stress field.

Once the shear bands spread throughout the system, the following steady flow will inevitably be influenced by the images of shear bands due to the periodic boundary condition. The smaller supercell size results in a greater overlap between the stress fields of the shear band and its images, and thus greatly suppresses its continued thickening. This leads to the appeared size-dependent thickness of shear bands after 10% strain as shown in Fig. 11. It is thus expected that as the computational supercell size increases, a longer stage of autocatalytic propagation, corresponding to a more significant stress drop after yielding, will be present, because a longer distance is needed to propagate before the shear band hits the boundary and the image-interaction starts to intervene.

4. Summary and outlook

The potential energy landscape (PEL) of atoms is a high-dimensional surface and very complex (Li et al., 2011). What we attempt to achieve in this paper is a reduction of the atomistic energy landscape in $\{\mathbf{x}_i\}$, where $\mathbf{x}_i$'s are atomic positions, to a *strain energy landscape* (SEL) in terms of voxel transformation strains ϵ^{ij}, where i, j index the 2D position of a voxel. Essentially, we developed here some kind of constitutive model for the strain energy landscape, a la Eshelby. Suppose each voxel contains ~10^2 atoms, we can achieve a factor of ~10^2 reduction in model dimension, and also direct visualization of voxel-level transformation strain and stress distribution, that could serve as a bridge to even coarser-level models. The assumptions underlying this dimensional reduction scheme is that diffusive motions of atoms is less important than the stress-driven, more collective displacive shear transformations. Some kind of diffusive recovery may underlie the recovery physics ("aging" Wolynes, 2009) in our model, but they are "enslaved" to the displacive transformations, and are most probable to happen soon after a displacive transformation. Like in any kind of constitutive modeling, we are beset by the complexity of the SEL. So we attempt to follow the principle of parsimony, where we only add parameters for which we see there is an absolute need.

In this current paper, we have developed a heterogeneously randomized STZ model to study strain localization and extreme value statistics during deformation of MGs. The model distinguishes itself from existing ones by including (a) heterogeneously randomized STZ transformation catalogs and (b) generation-dependent softening in kMC algorithm. Since information regarding (a) and (b), such as the STZ transformation modes, the transformation strain tensors, and the corresponding activation energy barriers, can in principle be obtained by detailed atomistic simulations, the model can be used in a multiscale scheme to study the effects of atomistic structure of MG on its deformation behavior.

Parametric simulation studies are carried out in two-dimensions using the model and statistical analysis on the probability density distribution and the extreme value in the Von Mises strain invariant are made. Both the simulation results

and the statistical analysis suggest a close relationship between the shear band formation and the internal structural information considered by new features in our model, and show the key role played by softening in strain localization and shear band formation. The thermal fluctuation and load-shedding elastic interaction, effects of which have been studied by previous STZ models, are found insufficient to cause strain localization under uniaxial tensile test considered in the simulations. In contrast, the generation-dependent softening results in an "autocatalytic" effect that is responsible for strain localization and is also likely to lead to abrupt fracture with limited ductility in reality. The thickness of the shear bands after nucleation is determined to be 18 nm, corresponding to the characteristic length of a cluster of 7 "diagonally aligned" transformed STZs. In addition, local temperature rise within a shear band is estimated and show that the center of shear bands could reach a temperature as high as over 3000 K at the single-voxel level. Since actual physical length is assigned to the STZ, the model, unlike other STZ models, is not "scale-free" and is able to describe size dependence, as has been demonstrated in the simulations.

In the presented model, the effect of voxel-level residual stress has been ignored, i.e. the starting states of all our voxels are assumed to be stress-free, which is different from what atomistic simulations indicated (Srolovitz et al., 1981; Egami, 2011). Imagine there is locked-in residual stress $\boldsymbol{\sigma}^{ij}$ on a particular voxel, then the voxel-level free energy landscape should be tilted on average in the voxel strain space (Fig. 2(a)), even when the externally applied stress $\bar{\boldsymbol{\sigma}}$ is zero. In other words, when voxel-level residual stress is considered, our constitutive model should generate "biased random", instead of "unbiased random", voxel-level SELs. Furthermore, the starting residual stress field must be self-balancing: $\nabla \cdot \boldsymbol{\sigma}_{\text{residual}} = 0$, so constraints like

$$\frac{\boldsymbol{\sigma}_{\text{residual}}^{i+1,j} - \boldsymbol{\sigma}_{\text{residual}}^{i-1,j}}{2\Delta x} + \frac{\boldsymbol{\sigma}_{\text{residual}}^{i,j+1} - \boldsymbol{\sigma}_{\text{residual}}^{i,j-1}}{2\Delta y} = 0 \tag{50}$$

must be satisfied. In other words, the tilting of voxel-level SELs on average must be coupled. Due to the complexity of adding such randomized but self-equilibrating $\{\boldsymbol{\sigma}_{\text{residual}}^{i,j}\}$, this effect is not considered in the present paper. We should pursue the effect of residual stress in future papers, as well generalizing the 2D results here to 3D.

Acknowledgements

Appendix A. Energetics for a spherical inclusion

Consider a simple case where the transformation at saddle-point can be decomposed into a simple shear part γ_* and pure dilatancy part ϵ^d:

$$\boldsymbol{\epsilon}_* = \begin{pmatrix} \epsilon^d/3 & \gamma_*/2 & 0 \\ \gamma_*/2 & \epsilon^d/3 & 0 \\ 0 & 0 & \epsilon^d/3 \end{pmatrix}. \tag{A.1}$$

The volume, under the first-order approximation, has the relationship $V_{g^*} \approx V_g(1 + \epsilon^d)$. We can then first obtain the resulted total strain energy following Eshelby (1957). For a nearly spherical cluster, Eshelby tensor is, according to Mura (1991):

$$\mathcal{S}_{ijkl} = \frac{5\nu - 1}{15(1 - \nu)}\delta_{ij}\delta_{kl} + \frac{4 - 5\nu}{15(1 - \nu)}(\delta_{ik}\delta_{jl} + \delta_{il}\delta_{jk}) \tag{A.2}$$

where ν is the Poisson's ratio and δ_{ij} is the Kronecker delta. The non-zero components of the constant stress field inside the inclusion are

$$\sigma_{11} = \sigma_{22} = \sigma_{33} = -\frac{4\mu(1 + \nu)}{9(1 - \nu)}\epsilon^d, \tag{A.3}$$

$$\sigma_{12} = \sigma_{21} = -\frac{\mu(7 - 5\nu)}{15(1 - \nu)}\gamma_*. \tag{A.4}$$

where μ is the shear modulus and Eq. (9) has been used to obtain the actual transformation strain ε_{ij}. The total strain energy after transformation $\boldsymbol{\epsilon}_*$ is then given by Eshelby (1957):

$$E_{\text{el}}^{\text{tot}} = -\frac{1}{2}\sigma_{ij}\epsilon_{ij}V_g. \tag{A.5}$$

This gives rise to the first two terms of activation energy barrier obtained by Argon (1979) and Argon and Shi (1983):

$$\Delta F_* = \left[\frac{7 - 5\nu}{30(1 - \nu)} + \frac{2(1 + \nu)}{9(1 - \nu)}\beta^2 + \frac{1}{2\gamma_*} \cdot \frac{\hat{\tau}}{\mu}\right]\mu\gamma_*^2 V_g \tag{A.6}$$

where $\beta = \epsilon^d/\gamma_*$ is the ratio of dilatancy at saddle-point, and $\hat{\tau}$ is the ideal shear resistance in a regular lattice (Argon, 1979). The third term comes from the work done against the resistance between interatomic layers up to the saddle-point (the

sinusoid-like form of shear resistance as a function of displacement is linearized to obtain the current form Argon (1979)). For more complicated cases, except for some special shapes (Mura, 1991), analytical solutions do not exist and numerical evaluation of elliptic integrals is usually needed.

Appendix B. Isotropically random strain matrix: 2D

The $\mathcal{M}$ SFTS tensors $\boldsymbol{\epsilon}^{(m)}$ for possible transformations in a generation change are numerically generated for our parametric studies. To physically represent the amorphous structure, we require our numerical approach to generate $\boldsymbol{\epsilon}$ such that the *distribution* is indistinguishable from that viewed in a rotated frame

$$\tilde{\boldsymbol{\epsilon}} = \mathbf{R}^T \boldsymbol{\epsilon} \mathbf{R} \tag{B.1}$$

where $\mathbf{R}$ is the rotation matrix. In the 2D case under the assumption of Eq. (5) and Eq. (9), we have

$$\boldsymbol{\epsilon} = \begin{pmatrix} \epsilon_1 & \epsilon_3 \\ \epsilon_3 & -\epsilon_1 \end{pmatrix}. \tag{B.2}$$

The rotation matrix in Eq. (B.1) for 2D becomes

$$\mathbf{R} = \begin{pmatrix} \cos\theta & -\sin\theta \\ \sin\theta & \cos\theta \end{pmatrix}, \tag{B.3}$$

with $\mathbf{R}\mathbf{R}^T = \mathbf{I}$, connecting $d\mathbf{x} = \mathbf{R}d\tilde{\mathbf{x}}$, and $(dl)^2 = d\mathbf{x}^T(\mathbf{I}+2\boldsymbol{\epsilon})d\mathbf{x} = d\tilde{\mathbf{x}}^T(\mathbf{I}+2\tilde{\boldsymbol{\epsilon}})d\tilde{\mathbf{x}}$. According to Eq. (B.1) we have

$$\tilde{\epsilon}_1 = [\cos\theta \quad \sin\theta]\begin{pmatrix} \epsilon_1 & \epsilon_3 \\ \epsilon_3 & -\epsilon_1 \end{pmatrix}\begin{bmatrix} \cos\theta \\ \sin\theta \end{bmatrix} = \epsilon_1\cos 2\theta + \epsilon_3\sin 2\theta. \tag{B.4}$$

$$\tilde{\epsilon}_3 = [\cos\theta \quad \sin\theta]\begin{pmatrix} \epsilon_1 & \epsilon_3 \\ \epsilon_3 & -\epsilon_1 \end{pmatrix}\begin{bmatrix} -\sin\theta \\ \cos\theta \end{bmatrix} = -\epsilon_1\sin 2\theta + \epsilon_3\cos 2\theta. \tag{B.5}$$

Because

$$\begin{bmatrix} \tilde{\epsilon}_1 \\ \tilde{\epsilon}_3 \end{bmatrix} = \begin{pmatrix} \cos 2\theta & \sin 2\theta \\ -\sin 2\theta & \cos 2\theta \end{pmatrix}\begin{bmatrix} \epsilon_1 \\ \epsilon_3 \end{bmatrix} \tag{B.6}$$

is a rotation transformation, we get the feeling that ϵ_1 and ϵ_3 are "equivalent" like $x-$ and $y-$ axis. Since a 2D Gaussian density cloud is obviously invariant after 2θ rotation, the proposal is to sample ϵ_1 and ϵ_3 from independent standard Gaussian distribution and then rescale them with the STZ characteristic shear $\gamma_*/2$ (the actual Gaussian width used in simulation, i.e. $0.1/2 = 0.05$ is consistent with atomistic simulations (Rodney and Schuh, 2009)). More generally, we could use arbitrary function $f(J_2)dJ_2$ to sample (ϵ_1, ϵ_3), where the J_2 invariant

$$J_2 \equiv -\det(\boldsymbol{\epsilon}) = \epsilon_1^2 + \epsilon_3^2 \tag{B.7}$$

is obviously an invariant under rotation, confirming our view that ϵ_1 and ϵ_3 are "equivalent" dimensions in strain space.

Appendix C. Elasticity solver: 2D isotropic media

A 2D isotropic medium has

$$c_{ijpq} = \lambda\delta_{ij}\delta_{pq} + \mu(\delta_{ip}\delta_{jq} + \delta_{iq}\delta_{jp}). \tag{C.1}$$

The relationship between the Lamé parameters λ, μ and E, v are:

$$\lambda = \frac{Ev}{1-v^2} = \frac{2v\mu}{1-v}, \quad \mu = \frac{E}{2(1+v)}, \tag{C.2}$$

and the relationship between stress-free stress $\boldsymbol{\sigma}^0$ and SFTS $\boldsymbol{\epsilon}$ is:

$$\sigma_{ij}^0(\mathbf{k}) = (\lambda\epsilon_{pp}(\mathbf{k}))\delta_{ij} + 2\mu\epsilon_{ij}(\mathbf{k}), \quad \sigma_{ij}^0(\mathbf{x}) = (\lambda\epsilon_{pp}(\mathbf{x}))\delta_{ij} + 2\mu\epsilon_{ij}(\mathbf{x}). \tag{C.3}$$

Then Eq. (35) becomes:

$$C_{ip}(\hat{\mathbf{k}}) = c_{ijpq}\hat{k}_j\hat{k}_q = \lambda\hat{k}_i\hat{k}_p + \mu\delta_{ip} + \mu\hat{k}_p\hat{k}_i = \mu\delta_{ip} + (\lambda+\mu)\hat{k}_i\hat{k}_p \tag{C.4}$$

or

$$\mathbf{C}(\hat{\mathbf{k}}) = \mu\mathbf{I} + (\lambda+\mu)\widehat{\mathbf{K}} \tag{C.5}$$

with $K_{ip} \equiv \hat{k}_i\hat{k}_p$. The $\widehat{\mathbf{K}}$ matrix is real and symmetric. It is also idempotent: $\widehat{\mathbf{K}}^n = \widehat{\mathbf{K}}$.

The inversion of $\mathbf{C}(\hat{\mathbf{k}})$ can be done by matrix series expansion:

$$\Omega(\hat{\mathbf{k}}) = \frac{1}{\mu}\sum_{n=0}^{\infty}\left(-\frac{\lambda+\mu}{\mu}\right)^n \widehat{\mathbf{K}}^n = \frac{1}{\mu}\left(\mathbf{I} - \frac{\lambda+\mu}{\mu}\frac{\widehat{\mathbf{K}}}{1+\frac{\lambda+\mu}{\mu}}\right) = \frac{1}{\mu}\left(\mathbf{I} - \frac{\lambda+\mu}{\lambda+2\mu}\widehat{\mathbf{K}}\right). \tag{C.6}$$

Define dimensionless quantity

$$\alpha \equiv \frac{\lambda+\mu}{\lambda+2\mu} = \frac{1+\nu}{2}, \tag{C.7}$$

we then have $\Omega(\hat{\mathbf{k}}) = (\mathbf{I} - \alpha\widehat{\mathbf{K}})/\mu$.

So Eq. (38) would become

$$\tilde{u}_p(\mathbf{k}) = \frac{(\delta_{pi'} - \alpha\hat{k}_p\hat{k}_{i'})\sigma^0_{i'j'}(\mathbf{k})\hat{k}_{j'}}{\mu i|\mathbf{k}|} = \frac{\sigma^0_{pj'}(\mathbf{k})\hat{k}_{j'} - \alpha\hat{k}_p\sigma^0_{i'j'}(\mathbf{k})\hat{k}_{i'}\hat{k}_{j'}}{\mu i|\mathbf{k}|}. \tag{C.8}$$

Define vector and scalar

$$\mathbf{f}(\mathbf{k}) \equiv \boldsymbol{\sigma}^0(\mathbf{k})\cdot\hat{\mathbf{k}}, \quad g(\mathbf{k}) \equiv \hat{\mathbf{k}}\cdot\mathbf{f}(\mathbf{k}), \tag{C.9}$$

which can be pre-computed, we then have

$$\tilde{\mathbf{u}}(\mathbf{k}) = \frac{\mathbf{f}(\mathbf{k}) - \alpha g(\mathbf{k})\hat{\mathbf{k}}}{\mu i|\mathbf{k}|}. \tag{C.10}$$

The periodic part of the actual strain field is then

$$\tilde{\boldsymbol{\varepsilon}}(\mathbf{k}) = \frac{i\tilde{\mathbf{u}}(\mathbf{k})\mathbf{k} + i\mathbf{k}\tilde{\mathbf{u}}(\mathbf{k})}{2} = \frac{\mathbf{f}(\mathbf{k})\hat{\mathbf{k}} + \hat{\mathbf{k}}\mathbf{f}(\mathbf{k}) - 2\alpha g(\mathbf{k})\widehat{\mathbf{K}}}{2\mu}, \tag{C.11}$$

with $\mathrm{tr}(\mathbf{f}(\mathbf{k})\hat{\mathbf{k}}) = \mathrm{tr}(\hat{\mathbf{k}}\mathbf{f}(\mathbf{k})) = \hat{\mathbf{k}}\cdot\mathbf{f}(\mathbf{k}) = g(\mathbf{k}), \mathrm{tr}(\tilde{\boldsymbol{\varepsilon}}(\mathbf{k})) = (1-\alpha)g(\mathbf{k})/\mu$, and

$$\boldsymbol{\varepsilon}(\mathbf{x}) = \bar{\boldsymbol{\varepsilon}} + \tilde{\boldsymbol{\varepsilon}}(\mathbf{x}), \quad \int d^3\mathbf{x}\tilde{\boldsymbol{\varepsilon}}(\mathbf{x}) = 0. \tag{C.12}$$

With this obtained total strain field, it is straightforward to get the corresponding stress field.

References

Argon, A., 1979. Plastic deformation in metallic glasses. Acta Metall. 27, 47.

Argon, A., 1996. Mechanical properties of single-phase crystalline media: deformation at low temperatures, In: Cahn, R., Hassen, P. (Eds.), Physical Metallurgy, North-Holland, Amsterdam, 3.21 Ed. pp. 1887.

Argon, A., Shi, L., 1983. Development of visco-plastic deformation in metallic glasses. Acta Metall. 31, 499.

Baret, J.C., Vandembroucq, D., Roux, S., 2002. Extremal model for amorphous media plasticity. Phys. Rev. Lett. 89, 195506.

Bei, H., Xie, S., George, E., 2006. Softening caused by profuse shear banding in a bulk metallic glass. Phys. Rev. Lett. 96, 105503.

Bian, Z., Pan, M., Zhang, Y., Wang, W., 2002. Carbon-nanotube-reinforced $Zr_52.5Cu_17.9Ni_14.6Al_10Ti_5$ bulk metallic glass composites. Appl. Phys. Lett. 81, 4739.

Bulatov, V., Argon, A., 1994. A stochastic model for continuum elasto-plastic behavior: I Numerical approach and strain localization. Model. Simul. Mater. Sci. Eng. 2, 167.

Chen, H., He, Y., Shiflet, G., Poon, S., 1994. Deformation-induced nanocrystal formation in shear bands of amorphous alloys. Nature 367, 541.

Donovan, P., Stobbs, W., 1981. The structure of shear bands in metallic glasses. Acta Metall. 29, 1419.

Dubach, A., Dalla Torre, F., Löffler, J., 2007. Deformation kinetics in zr-based bulk metallic glasses and its dependence on temperature and strain-rate sensitivity. Philos. Mag. Lett. 87, 695.

Egami, T., 2011. Atomic level stresses. Prog. Mater. Sci. 56, 637–653.

Eshelby, J., 1957. The determination of the elastic field of an ellipsoidal inclusion, and related problems. Proc. R. Soc. Lond. Ser. A-Math. 241, 376.

Falk, M., Langer, J., 1998. Dynamics of viscoplastic deformation in amorphous solids. Phys. Rev. E 57, 7192.

Fisher, R.A., Tippett, L.H.C., 1928. Limiting forms of the frequency distribution of the largest or smallest member of a sample. P. Camb. Philos. Soc. 24, 180–190.

Hara, S., Li, J., 2010. Adaptive strain-boost hyperdynamics simulations of stress-driven atomic processes. Phys. Rev. B 82, 184114.

Hirata, A., Guan, P., Fujita, T., Hirotsu, Y., Inoue, A., Yavari, A., Sakurai, T., Chen, M., 2011. Direct observation of local atomic order in a metallic glass. Nature Mater. 10, 28.

Hofmann, D., Suh, J., Wiest, A., Duan, G., Lind, M., Demetriou, M., Johnson, W., 2008. Designing metallic glass matrix composites with high toughness and tensile ductility. Nature 451, 1085.

Homer, E., Schuh, C., 2009. Mesoscale modeling of amorphous metals by shear transformation zone dynamics. Acta Mater. 57, 2823.

Homer, E., Schuh, C., 2010. Three-dimensional shear transformation zone dynamics model for amorphous metals. Model. Simul. Mater. Sci. Eng. 18, 065009.

Hufnagel, T., Jiao, T., Li, Y., Xing, L., Ramesh, K., 2002. Deformation and failure of $Zr_57Ti_5Cu_20Ni_8Al_10$ bulk metallic glass under quasi-static and dynamic compression. J. Mater. Res. 17, 1441.

Jiang, W., Atzmon, M., 2003. The effect of compression and tension on shear-band structure and nanocrystallization in amorphous $Al_90Fe_5Gd_5$: a high-resolution transmission electron microscopy study. Acta Mater. 51, 4095.

Johnson, W., Samwer, K., 2005. A universal criterion for plastic yielding of metallic glasses with a $(T/T_g)^2/3$ temperature dependence. Phys. Rev. Lett. 95, 195501.

Khachaturyan, A., 1983. Theory of Structural Transformations in Solids. John Wiley & Sons, New York.

Kim, J., Choi, Y., Suresh, S., Argon, A., 2002. Nanocrystallization During Nanoindentation of a Bulk Amorphous Metal Alloy at Room Temperature. Science, 295, 654.

Kushima, A., Lin, X., Li, J., Eapen, J., Mauro, J.C., Qian, X.F., Diep, P., Yip, S., 2009. Computing the viscosity of supercooled liquids. J. Chem. Phys. 130, 224504.

Lewandowski, J., Greer, A., 2006. Temperature rise at shear bands in metallic glasses. Nature Mater. 5, 15.

Li, J., 2007. The mechanics and physics of defect nucleation. MRS Bull. 32, 151–159.
Li, J., 2000. Modeling Microstructural Effects on Deformation Resistance and Thermal Conductivity. Ph.D. thesis, Massachusetts Institute of Technology, August.
Li, J., Kushima, A., Eapen, J., Lin, X., Qian, X.F., Mauro, J.C., Diep, P., Yip, S., 2011. Computing the viscosity of supercooled liquids: Markov network model. PLoS One 6, e17909.
Li, J., Ngan, A.H.W., Gumbsch, P., 2003. Atomistic modeling of mechanical behavior. Acta Mater. 51, 5711–5742.
Li, Jing., Spaepen, F., Hufnagel, T., 2002. Nanometre-scale defects in shear bands in a metallic glass. Philos. Mag. A 82, 2623.
Mayr, S., 2006. Activation energy of shear transformation zones: a key for understanding rheology of glasses and liquids. Phys. Rev. Lett. 97, 195501.
Mura, T., 1991. Micromechanics of Defects in Solids, Second revision Ed. Kluwer Academic Publishers.
Nagendra, N., Ramamurty, U., Goh, T., Li, Y., 2000. Effect of crystallinity on the impact toughness of a La-based bulk metallic glass. Acta Mater. 48, 2603.
Neuhauser, H., 1978. Rate of shear band formation in metallic glasses. Scripta Metall. 12, 471.
Packard, C., Schuh, C., 2007. Initiation of shear bands near a stress concentration in metallic glass. Acta Mater. 55, 5348.
Pampillo, C., 1975. Flow and fracture in amorphous alloys. J. Mater. Sci. 10, 1194.
Pan, D., Inoue, A., Sakurai, T., Chen, M., 2008. Experimental characterization of shear transformation zones for plastic flow of bulk metallic glasses. Proc. Natl. Acad. Sci. USA 105, 14769.
Pekarskaya, E., Kim, C., Johnson, W., 2001. In situ transmission electron microscopy studies of shear bands in a bulk metallic glass based composite. J. Mates. Res. 16, 2513.
Pickands, J., 1975. Statistical-inference using extreme order statistics. Ann. Stat. 3, 119–131.
Reiss, R.D., Thomas, M., 2007. Statistical Analysis of Extreme Values: with Applications to Insurance. Finance. Hydrology and Other Fields. Birkhauser, Basel.
Ritchie, R.O., 2011. The conflicts between strength and toughness. Nat. Mater. 10, 817–822.
Rodney, D., Schuh, C., 2009. Distribution of thermally activated plastic events in a flowing glass. Phys. Rev. Lett. 102, 235503.
Rodney, D., Tanguy, A., Vandembroucq, D., 2011. Modeling the mechanics of amorphous solids at different length scale and time scale. Model. Simul. Mater. Sci. Eng. 19, 083001.
Rogers, H., 1979. Adiabatic plastic deformation. Ann. Rev. Mater. Sci. 9, 283.
Schuh, C., Hufnagel, T., Ramamurty, U., 2007. Mechanical behavior of amorphous alloys. Acta Mater. 55, 4067.
Schuh, C.A., Lund, A.C., 2003. Atomistic basis for the plastic yield criterion of metallic glass. Nat. Mater. 2, 449–452.
Sciortino, F., Kob, W., Tartaglia, P., 1999. Inherent structure entropy of supercooled liquids. Phys. Rev. Lett. 83, 3214–3217.
Sethi, V., Gibala, R., Heuer, A., 1978. Transmission electron microscopy of shear bands in amorphous metallic alloys. Scripta Metall. 12, 207.
Shan, Z.W., Li, J., Cheng, Y.Q., Minor, A.M., Asif, S.A.S., Warren, O.L., Ma, E., 2008. Plastic flow and failure resistance of metallic glass: insight from in situ compression of nanopillars. Phys. Rev. B 77, 155419.
Shimizu, F., Ogata, S., Li, J., 2006. Yield point of metallic glass. Acta Mater. 54, 4293–4298.
Shimizu, F., Ogata, S., Li, J., 2007. Theory of shear banding in metallic glasses and molecular dynamics calculations. Mater. Trans. 48, 2923–2927.
Spaepen, F., 1977. A microscopic mechanism for steady state inhomogeneous flow in metallic glasses. Acta Metall. 25, 407.
Srolovitz, D., Egami, T., Vitek, V., 1981. Radial-distribution function and structural relaxation in amorphous solids. Phys. Rev. B 24, 6936–6944.
Srolovitz, D., Vitek, V., Egami, T., 1983. An atomistic study of deformation of amorphous metals. Acta Met 31, 335–352.
Steif, P., Spaepen, F., Hutchinson, J., 1982. Strain localization in amorphous metals. Acta Metall. 30, 447.
Stillinger, F.H., Weber, T.A., 1982. Hidden structure in liquids. Phys. Rev. A 25, 978–989.
Su, C., Anand, L., 2006. Plane strain indentation of a zr-based metallic glass: experiments and numerical simulation. Acta Mater. 54, 179.
Suzuki, Y., Haimovich, J., Egami, T., 1987. Bond-orientational anisotropy in metallic glasses observed by x-ray diffraction. Phys. Rev. B 35, 2162.
Takeuchi, S., Edagawa, K., 2011. Atomistic simulation and modeling of localized shear deformation in metallic glasses. Prog. Mater. Sci. 56, 785.
Tian, L., Cheng, Y.Q., Shan, Z.W., Li, J., Wang, C.C., Han, X.D., Sun, J., Ma, E., 2012. Approaching the ideal elastic limit of metallic glasses. Nature Commun. 3, 609.
Trexler, M., Thadhani, N., 2010. Mechanical properties of bulk metallic glasses. Prog. Mater. Sci. 55, 759.
Utz, M., Debenedetti, P., Stillinger, F., 2000. Atomistic simulation of aging and rejuvenation in glasses. Phys. Rev. Lett. 84, 1471.
Vaidyanathan, R., Dao, M., Ravichandran, G., Suresh, S., 2001. Study of mechanical deformation in bulk metallic glass through instrumented indentation. Acta Mater. 49, 3781.
Vandembroucq, D., Roux, S., 2011. Mechanical noise dependent aging and shear banding behavior of a mesoscopic model of amorphous plasticity. Phys. Rev. B 84, 134210.
Voter, A., 2007. Introduction to the kinetic Monte Carlo method. In: Sickafus, K., Kotomin, E., Uberuaga, B. (Eds.), Radiation effects in solids. Springer.
Wang, Y., Li, J., 2010. Phase field modeling of defects and deformation. Acta Mater. 58, 1212.
Wang, Yu U., Jin, Y., Khachaturyan, A., 2002. Phase field microelasticity theory and modeling of elastically and structurally inhomogeneous solid. J. Appl. Phys. 92, 1351.
Wolynes, P.G., 2009. Spatiotemporal structures in aging and rejuvenating glasses. Proc. Natl. Acad. Sci. USA 106, 1353–1358.
Xi, X., Zhao, D., Pan, M., Wang, W., Wu, Y., Lewandowski, J., 2005. Fracture of brittle metallic glasses: brittleness or plasticity. Phys. Rev. Lett. 94, 125510.
Yang, B., Morrison, M., Liaw, P., Buchanan, R., Wang, G., Liu, C., Denda, M., 2005. Dynamics evolution of nanoscale shear bands in a bulk-metallic glass. Appl. Phys. Lett. 86, 141904.
Yang, Q., Mota, A., Ortiz, M., 2006. A finite-deformation constitutive model of bulk metallic glass plasticity. Comput. Mech. 37, 194.
Zhang, Y., Greer, A., 2006. Thickness of shear bands in metallic glasses. Appl. Phys. Lett. 89, 071907.
Zhao, P., Li, J., Wang, Y., submitted for publication.
Zhu, T., Li, J., 2010. Ultra-strength materials. Prog. Mater. Sci. 55, 710–757.